A Practical and Reliable Method for Volumetric Assessment of Adult Diffuse Glioma Features on MRI

by

Maya Willms

Submitted in partial fulfilment of the requirements
for the degree of Master of Science

at

Dalhousie University
Halifax, Nova Scotia
December, 2021

TABLE OF CONTENTS

LIST OF TABLES

LIST OF FIGURES

ABSTRACT

Background: The purpose of this study was to develop a reliable volumetric assessment of MRI-based tumour features, using available clinical software, to track tumour features longitudinally in patients with adult diffuse gliomas, and to assess the correlation between tumour features and biomarkers obtained by liquid biopsy.

Methods: A manual segmentation protocol was developed to quantify tumour volumes and diffusion restricted volumes on serial MRIs. These measures were assessed longitudinally and then correlated with liquid biopsy derived RNA concentrations.

Results: The segmentation technique has high reliability and can be used to track tumour volumes longitudinally. Significant correlations were found between diffusion restricted tissue and RNA concentrations in contrast enhanced and gross tumour regions.

Conclusions: This technique is suitable for longitudinal studies of novel biomarkers of tumour progression and post-treatment recurrence. Further study is indicated on the relationship between diffusion restriction and clinical course, as well as the correlation with RNA concentration.

LIST OF ABBREVIATIONS USED

ADC	Apparent Diffusion Coefficient
ASL	Arterial Spin Labelling
BBB	Blood-Brain-Barrier
CE	Contrast Enhanced
DCE	Dynamic Contrast-Enhanced T1w imaging
DSC	Dynamic Susceptibility Contrast-Enhanced imaging
DWI	Diffusion Weighted Imaging
ETL	Echo Train Length
EV	Extracellular Vesicle
FA	Flip Angle
FLAIR	Fluid Attenuated Inversion Recovery
FOV	Field of View
FSE	Fast Spin Echo
GBM	Glioblastoma Multiforme
GT	Gross Tumour
ICC	Intraclass Correlation Coefficient
IDH	Isocitrate Dehydrogenase
MGMT	O6-methylguanine-DNA methyltransferase
MRI	Magnetic Resonance Imaging
MRS	Magnetic Resonance Spectroscopy
MVP	Microvascular Proliferation
NEX	Number of Excitations
PROPELLER	Periodically Rotated Overlapping Parallel Lines with Enhanced Reconstruction
PsP	Pseudoprogression
RANO	Response Assessment in Neuro-Oncology
rCBF	Relative Cerebral Blood Flow
rCBV	Relative Cerebral Blood Volume
RF	Radiofrequency Pulse
RNA	Ribonucleic Acid
ROI	Region of Interest
SSFSE	Single Shot Fast Spin Echo
T1w	T1 weighted
T2w	T2 weighted
TE	Echo Time
TI	Inversion Time
TMZ	Temozolomide
TR	Repetition Time

ACKNOWLEDGEMENTS

I would like to give special acknowledgments to my supervisors Dr. Matthias Schmidt and Dr. Adrienne Weeks who have been exceptional mentors and a great inspiration. I would also like to thank all the Weeks lab members who have contributed greatly to this project, including Dr. Jeremy Roy, Andrea Hebb, Kathleen Atwood, Liam Rappolt, Jae Han and Emma Gilllespie-Fraser. I would like to thank the following people for their helpful comments during the review process and extensive training throughout this project: Dr. Matthias Schmidt, Dr. Adrienne Weeks, Dr. Chris Bowen, Dr. Sidney Croul and Dr. Kazue Semba. This study would not be possible without their support.

This thesis is written by Maya Willms and complies with Dalhousie University's regulations on plagiarism.

CHAPTER 1 INTRODUCTION

1.1 Biology and Classification of Adult Gliomas

Gliomas are malignant brain tumours of astrocytic, oligodendroglial or ependymal origin (Louis et al., 2021). Together, they account for 80% of malignant brain tumours in adults (Goodenberger & Jenkins, 2012). Gliomas are graded according to the World Health Organization's classification for central nervous system tumours (WHO CNS5) on the basis of their clinical and biological behaviour (Louis et al., 2021). Traditionally, WHO grades 2 and 3 are assigned to gliomas with anaplasia and mitotic activity, whereas grade 4 is assigned to gliomas that also demonstrate microvascular proliferation or necrosis (Louis et al., 2007). The majority of gliomas (54%) are the grade 4 Glioblastoma Multiforme (GBM), which is the most aggressive malignant brain cancer (Ostrom et al., 2013; Urbańska et al., 2014).

More recently, the classification of gliomas has come to be based on integrated histology and molecular markers (Louis et al., 2021). Genome-wide molecular profiling studies have elucidated the importance of genetic factors in tumorigenesis and prognosis (Cancer Genome Atlas Research Network, 2015; Reifenberger et al., 2017). The incorporation of molecular markers such as mutations in isocitrate dehydrogenase (IDH) has been instrumental to an integrated approach to brain tumour diagnosis and has refined classification of adult diffuse gliomas, as depicted in Figure 1. For adult diffuse gliomas, tumours are now classified as 3 types: (1) Oligodendroglioma, IDH-

mutant, 1p/19q co-deleted; (2) Astrocytoma, IDH-mutant; and (3) Glioblastoma, IDH-wildtype (Louis et al., 2021).

Molecular biomarkers such as IDH-mutation status have shown to have a better correlation with prognosis than histological features (Reifenberger et al., 2017). IDH mutations cause aberrant DNA and histone methylation, and are among the earliest genetic aberrations in glioma development (Wick et al., 2013). IDH mutations are known to occur in approximately 60-80% of gliomas and are typically associated with better outcome, partly owing to the younger median age of patients at diagnosis (Wick et al., 2013; Reifenberger et al., 2017).

With respect to determining astrocytic or oligodendroglial origin, molecular markers now outweigh histological features (Louis et al., 2021). Oligodendrogliomas have co-deletions of chromosome 1 (1p) and chromosome 19 (19q), which is now considered a defining feature (Yip et al., 2012). The 1p/19q co-deletion is also associated with better clinical outcomes, as well as being an important distinguishing feature from astrocytomas (Yip et al., 2012). Oligodendrogliomas are graded as 2 or 3 and have a median survival time of 10-12 years (El-Hateer et al., 2009).

Astrocytoma IDH mutant diffuse gliomas can be graded as 2, 3 or 4, with grade 4 assigned to a tumour with any of the following features: microvascular proliferation (MVP), necrosis or homozygous deletion of the CDKN2A/B gene locus (Louis et al., 2021; Weller et al., 2021). Astrocytoma IDH-mutant diffuse gliomas also characteristically

show loss of nuclear expression ATRX and mutations in the tumour protein 53 (TP53) gene (Weller et al., 2021).

Lastly, GBM IDH-wildtype is always considered to be a grade 4 glioma, arising either as a primary GBM (90%) or as a secondary GBM (10%), due to the malignant transformation of a lower grade astrocytoma or oligodendroglioma (Urbańska et al., 2014). One of the hallmarks of GBM is neovascularity and breakdown of the blood brain-barrier (BBB) (Kim and Lee, 2009). When GBMs reach a critical mass, typically around 1-2cm in diameter, they recruit additional blood vessels to compensate for their rapid growth and the hypoxic intratumoural environment (Kim and Lee, 2009). GBM angiogenesis is accomplished by secreting proangiogenic signalling molecules such as vascular endothelial growth factor (VEGF), which remain consistently active within the tumour microenvironment (Good et al., 1990). This perpetual signalling facilitates rapid microvascular proliferation of endothelial cells, allowing the tumour to recruit large amounts of new blood vessels by exploiting pre-existing vasculature (Good et al., 1990). The rapid proliferation leads to structural consequences in the surrounding vasculature, producing highly permeable and irregular new blood vessels (Ahir et al., 2020). The neovascularity further facilitates the tumour's growth and compromises the BBB (Ahir et al., 2020). In addition to microvascular proliferation and/or necrosis, genetic and molecular alterations such as TERT promoter mutation, epidermal growth factor receptor (EGFR) gene amplification and the combined gain of chromosome 7 and loss of chromosome 10 (+7/−10) are also used in the diagnosis of Glioblastoma IDH-wildtype (Louis et al., 2021).

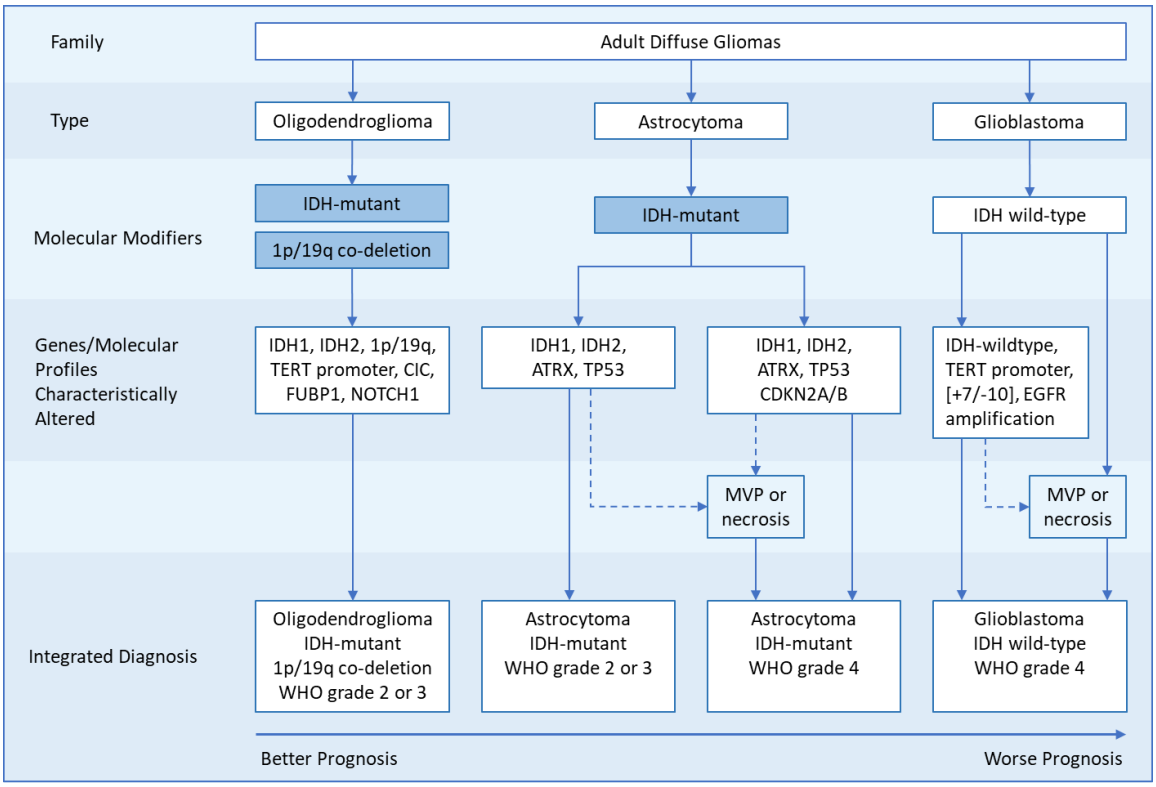

Figure 1. Diagnostic schema for diffuse gliomas.
Glioma classifications based on the 2021 WHO classification of tumours of the central nervous system 5 (Louis et al., 2021). MVP, microvascular proliferation.

1.1.1 Clinical Presentation and Survival Rates

Presentation of gliomas often includes constitutional symptoms such as fatigue and nausea, as well as headaches due to increased intracranial pressure (Urbańska et al., 2014). Depending on the location of the tumour, cognitive deficits or seizures may occur (McKinnon et al., 2021). Neurological symptoms such as impairment of memory, attention and executive functioning result from disruption of healthy areas of the brain, and this may be exacerbated by edema (Dallabona et al., 2017).

Peritumoural edema is frequently seen in patients with high grade gliomas and contributes significantly to neurological symptoms (Schoenegger et al., 2009). Extensive

edema may also contribute to shorter survival times; however, this has been debated (Lacroix et al., 2001; Schoenegger et al., 2009; Pope et al., 2005). Regardless, it is well established that neoplastic infiltration of malignant cancer cells is present within glioma related edema (Leao et al., 2020).

The physical changes to the brain due to the rapid proliferation of cancer cells ultimately leads to neurological deterioration and is universally fatal (Abler et al., 2018; Mitra et al., 2016).

The survival rate following diagnosis of a malignant glioma varies depending on classification and generally decreases with older age at diagnosis (Ostrom et al., 2020). Oligodendrogliomas have the highest five-year relative survival rate (up to 83.4%) among all gliomas (Ostrom et al., 2020). For astrocytomas, the five-year relative survival rate ranges from 31.1-53% depending on grade and age (Ostrom et al., 2020). Finally, GBMs have the lowest five-year relative surivival rate of any malignant central nervous system tumour (7.2% for all ages), with a median survival of 8 months from time of diagnosis regardless of treatment (Ostrom et al., 2020; Stupp et al., 2005). The median age at diagnosis for GBM is 64-65 years, and among patients older than 40 years, only 5.9% live past 5 years (Ostrom et a., 2020; Stupp et al., 2005; Lacroix et al., 2001). Those who live beyond 5 years with a GBM diagnosis are considered to be long term survivors (Krex et al., 2007).

1.1.2 The Current Clinical Standard for Treatment

Treatment for high grade gliomas is multimodal and aggressive, due to the invasive nature of these tumours. The current standard of treatment for GBMs consists of maximal surgical resection that is safely achievable, followed by local radiotherapy with concomitant chemotherapy and adjuvant chemotherapy using temozolomide (TMZ) (Stupp et al., 2005; Stupp et al., 2009; Van Dijken et al., 2017). TMZ is an oral alkylating agent that functions by sensitizing tumour cells to radiation and has shown to be critical in improving overall survival (Stupp et al., 2005). In a randomized clinical trial of 573 patients with high grade gliomas, there was a significant increase in overall survival for patients receiving concomitant TMZ and radiation (14.6 months) compared to those receiving radiation alone (12.1) (Stupp et al., 2005).

In lower grade gliomas, optimal treatment is controversial, as management must balance the benefits of therapeutic intervention with side effects of the treatment. First, maximal safe resection is performed, when possible, in order to reduce mass effect and edema and their associated neurological symptoms (Palombi et al., 2018). Decisions regarding subsequent treatment with chemoradiotherapy must then weigh the risk of cumulative neurotoxicity and radiation-induced edema, which can lead to long term deficits in memory and cognition (Klein et al., 2012). These adverse effects are especially unfavourable for younger patients with lower grade gliomas, as these patients are expected to have longer progression free survival times (5-10 years) (Ostrom et al., 2020). In order to minimize cumulative neurotoxicity and preserve cognitive function, post-operative treatment may be delayed until imaging shows signs of progression

(Wang et al., 2019). Once progression is evident, chemoradiotherapy can be used to slow malignant transformation into a higher-grade glioma (Wang et al., 2019).

Following chemoradiotherapy, cerebral edema is a common side effect of treatment. Cerebral edema is treated with dexamethasone, a glucocorticoid with anti-inflammatory and immunosuppressant properties, which has been shown to reduce the neurological symptoms produced by edema (Palombi et al., 2018). In a large cohort study of 459 patients undergoing radiochemotherapy, patients that had adjuvant dexamethasone suffered significantly fewer neurological symptoms than those with radiochemotherapy alone (Palombi et al., 2018). However, while dexamethasone may alleviate neurological systems associated with aggressive treatment, there is evidence that its concurrent use with chemoradiotherapy negatively impacts overall survival (Shields et al., 2015).

Epigenetic factors influence treatment response, most notably the methylation status of the promoter site of the gene for the DNA-repair enzyme O6-methylguanine-DNA methyltransferase (MGMT) (Stupp et al., 2005). MGMT rescues cancer cells from damage induced by chemotherapeutic alkylating agents, resulting in tumour resistance (Weller et al., 2010). The MGMT promotor can exist in methylated and unmethylated states, and methylation status differs among tumours (Chai et al., 2021). Gliomas with MGMT-promotor methylation have low levels of the repair enzyme, making them sensitive to treatment with TMZ, which in turn sensitizes cells to radiation (Chamberlain et al., 2007). This is particularly important for patients with low tolerance to aggressive chemoradiation regimens. MGMT methylation is thus associated with better outcomes

and longer survival times and can be used to guide treatment decisions in order to prevent unnecessary treatment toxicities (Weller et al., 2015; Weller et al., 2021).

In addition to methylation status, extent of surgical resection is an important prognostic indicator for overall survival. Resection of 89% or more has shown to be necessary to improve survival outcome (Lacroix et al., 2001). In a retrospective clinical study of 416 patients undergoing surgical resection for GBM, it was shown that resections of 98% or more of the tumour volume give a significant survival advantage (13 months vs. 8.8-10.1 months for resections <98%) (Lacroix et al., 2001).

Despite maximal surgical resection, the diffuse infiltration of GBMs into surrounding areas of the brain limits their complete surgical resection, making tumour recurrence inevitable (Wick et al., 2014). Even with the most aggressive treatment, roughly 90% of GBMs will recur in the same location and the median overall survival following diagnosis of tumour recurrence is approximately 6.5 months due to limited effective treatment options (Stupp et al., 2005; Van Linde et al., 2017). The diagnosis of tumour recurrence is complicated by the overlapping appearance of treatment effects.

1.2 Role of Magnetic Resonance Imaging in the Detection and Monitoring of Adult Gliomas

The detection and surveillance of brain gliomas relies heavily on magnetic resonance imaging (MRI). MRI is used for initial diagnosis, to assess the extent of surgical resection and to monitor for recurrence after treatment (Van Dijken et al., 2017). Adequate

imaging is crucial for clinical decisions regarding the continuation or discontinuation of treatment plans for individuals with gliomas.

MRI provides a non-invasive means for visualizing tissues within the body, based on the exploitation of magnetic relaxation properties that vary among different tissues (Argentieri et al., 2020). When placed in a strong external magnetic field, hydrogen nuclei (protons) within the body align with the z axis of the magnetic field (B_0) (Fig. 2a) (Mastrogiacomo et al., 2019). Specifically, protons align parallel or antiparallel to B_0. As the parallel orientation is more energetically favourable, a slight majority align in this orientation, producing a net magnetic vector (M_0) parallel to B_0 (Fig. 2a). A radiofrequency pulse (RF) can then be used to excite the protons, tilting M_0 by a specific degree based on the pulse. Once the RF pulse is switched off, the time it takes for the excited nuclei to return to equilibrium along the axis of the main magnetic field can be measured to produce tissue contrasts (weighting), namely T1-weighted (T1w) and T2-weighted (T2w) images (Sharma, 2009). T1 relaxation time (also known as spin-lattice) is the time it takes for the magnetism along the z axis to recover to 63% of its original value, and is affected by the protons' ability to release their kinetic energy to the surrounding environment (Fig. 1b) (Mastrogiacomo et al., 2019). T2 relaxation time (spin-spin) is the time it takes for the magnetism along the transverse (x-y) plane to decay (dephase) to 37% of its initial value, and is determined by the ability of the protons to exchange energy with each other (Fig. 2c) (Argentieri et al., 2020; Mastrogiacomo et al., 2019).

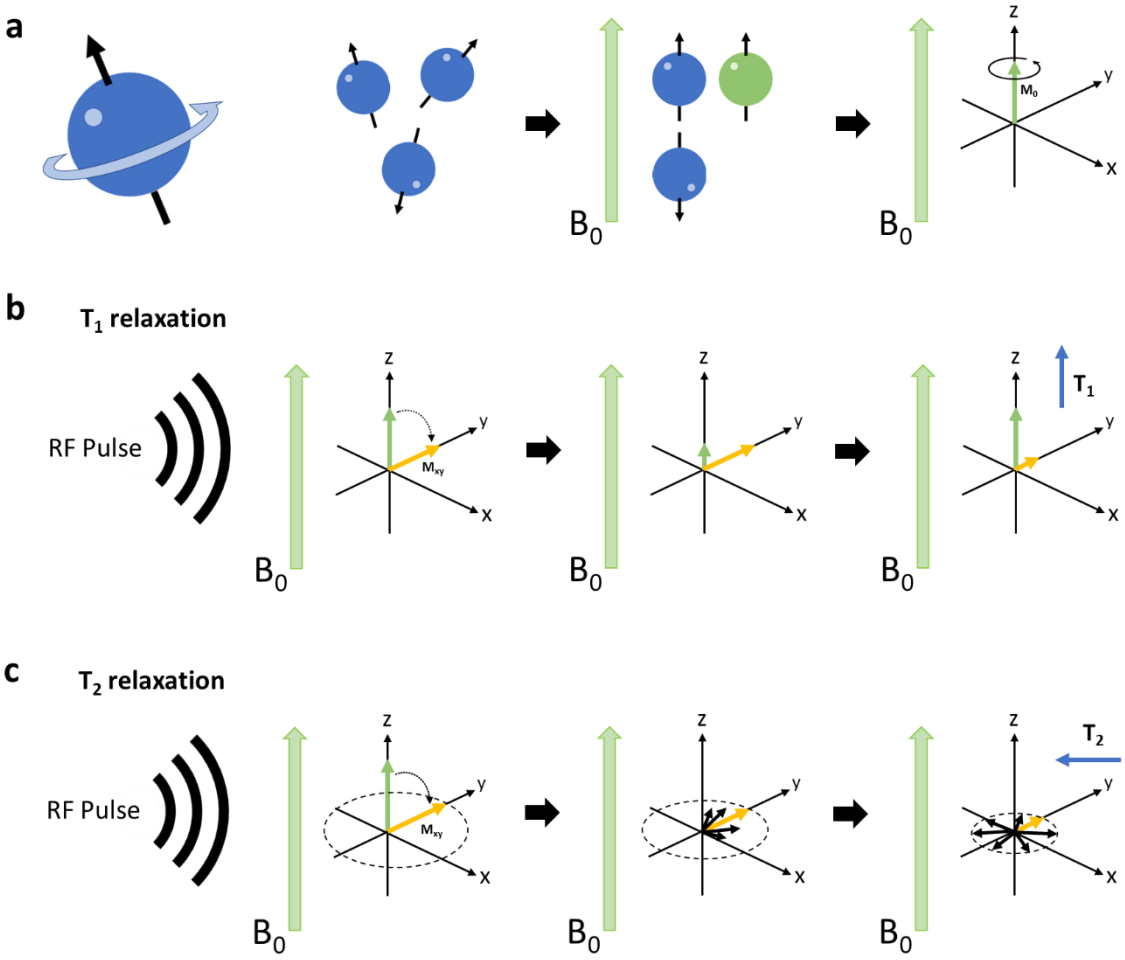

Figure 2. Basic MRI Principles.
a) Protons spinning around their own axis are magnetized along an external magnetic field (B_0). The sum of parallel and anti-parallel spins produces a net magnetization vector (M_0). A 90° radiofrequency pulse (RF) is applied, tilting M_0 into the transverse plane (M_{xy}). When the RF pulse is removed, M M_{xy} returns to equilibrium through T1 (b) and T2 relaxation (c). **b)** T1 relaxation is the time required to reach 63% of the original longitudinal magnetization. **c)** T2 relaxation is the time required for M_{xy} to dephase to 37% of the original value. Figure based on Mastrogiacomo et al., 2019.

The RF pulse sequence can be modified by changing the interval between pulses (repetition time; TR) or the interval between the applied pulse and the peak of the returning signal (echo time; TE) in order to produce image contrasts (Mastrogiacomo et al., 2019). With a long TR, protons have enough time to realign with the magnetic field,

minimizing T1 contrast. Likewise, with a short TE, there is little time for the signal to decay, minimizing T2 contrast (Mastrogiacomo et al., 2019). Therefore, a short TR and short TE is used to generate a T1w image and a long TR and long TE is used to generate a T2w image. Based on the free water content, the macromolecular environment and the structural characteristics of tissues, the relaxation time differs between tissue types, allowing them to be distinguished with MRI (Westbrook & Talbot, 2019). Tissues with high free water content have long relaxation times, producing a stronger MR signal, whereas tissue with low free water content have rapid signal decay and appear darker on imaging (Argentieri et al., 2020). The pulse sequence used to generate T1w and T2w images in this manner is called spin-echo (SE) and uses a 90^{o} pulse followed by a 180^{o} inversion pulse (Bitar et al., 2006). In addition, an inversion-recovery pulse can be used to supress the signal from free water, such as cerebrospinal fluid (CSF), producing a Fluid Attenuated Inversion Recovery (FLAIR) image (Bitar et al., 2006). The signal intensities of various tissues within the brain are summarized in Table 1 for T1w, T2w and FLAIR images.

Table 1. T1w, T2w and FLAIR image signal strength for various tissues within the brain.

Tissue Type	T1w	T2w	FLAIR
Cerebrospinal Fluid	Dark	Bright	Dark
White Matter	Intermediate-Bright	Intermediate-Dark	Intermediate-Dark
Grey Matter	Intermediate-Dark	Intermediate-Bright	Intermediate-Bright
Fat	Bright	Bright	Bright
Edema	Dark	Bright	Bright
Cyst	Dark	Bright	Dark
Bone	Dark	Dark	Dark

Gadolinium-based contrast enhancing agents can be used to increase T1 signal wherever the contrast enhancing agent accumulates, producing preferential tissue enhancement (Ibrahim et al., 1998). This is accomplished by the paramagnetic properties of the rare earth metal, which increases the magnetic susceptibility of a tissue, thus shortening T1 relaxation time and subsequently increasing MRI signal (Ibrahim et al., 1998). Contrast enhancing agents are injected intravenously and pool in regions of disrupted BBB, making them useful for detecting and characterizing brain tumours that have a compromised BBB (Westbrook & Talbot, 2019). Tumour progression, transformation of lower grade gliomas to higher grade gliomas and treatment response are traditionally examined on contrast enhanced T1w MRI and T2w/FLAIR MRI; however, more advanced techniques have allowed further tumour features to be examined (Van Dijken et al., 2017).

Using advanced MRI techniques, tumour parameters such diffusion restriction, relative cerebral blood volume and blood flow can be examined on diffusion-weighted and perfusion weighted imaging, respectively (Van Dijken et al., 2017). This thesis will primarily focus on three MRI parameters: contrast-enhanced tumour tissue, T2 FLAIR hyperintensity and diffusion restriction.

Diffusion-weighted imaging (DWI) can be used to evaluate changes in cellular density, by measuring the random movement of water molecules within a tissue (Kwee et al., 2010). Presence of cellular structures, such as cell membranes, restricts the free movement of water molecules and levels of diffusion restriction vary depending on a tissue's cytoarchitecture.

To obtain diffusion information, diffusion sensitizing gradients are applied during image acquisition. The degree of diffusion sensitization is expressed as the b-value, with higher values denoting greater diffusion weighting. First, a b=0 image is acquired as a baseline. Then, images with a higher b-value are acquired in at least 3 mutually orthogonal directions (x, y and z) by applying two equal and symmetrical strong gradients on either side of the 180^{o} RF pulse to generate transverse magnetization (Westbrook & Talbot, 2019). The first gradient dephases stationary water molecules, whereas the second gradient rephases them, undoing the effect (Westbrook & Talbot, 2019). Thus, stationary water molecules retain their signal. Water molecules that are moving will not be in the same location once the second gradient is applied and will not be rephased to the same degree that they were dephased, resulting in a loss of signal (Bitar et al., 2006). The further water molecules move, the more signal is lost. The most commonly used pulse sequences to create DWI are the spin-echo echo-planar sequence (SE-EPI) and gradient echo (GRE) sequence (Bitar et al., 2006).

Apparent diffusion coefficients (ADC) can be calculated from DWI and used to quantify the diffusion restriction within each individual voxel (Orlandi et al., 2016). ADC is an estimate of the mean diffusivity, measured in mm^2/s, which enables tissue cellularity to be assessed non-invasively (Kwee et al., 2010). Regions of high cellular density exhibit low ADC values, whereas regions of low cellular density show high ADC values (Kwee et al., 2010).

1.2.1 Glioma Appearance on Conventional MRI Contrasts

Adult diffuse gliomas have similar appearances on MRI, however there are some key differences between classifications.

GBMs typically appear as a mass lesion with a heterogeneous hypointense necrotic cavity and an irregular rim of contrast-enhancing tissue on T1w images (Leao et al., 2020). The appearance of an enhancing rim is due to gadolinium pooling in areas of disrupted BBB, reflecting tumour vascularity and angiogenesis (Ibrahim et al., 1998). The non-enhancing portion of the tumour and peritumoural vasogenic edema are best observed on T2w and FLAIR MRI sequences and will appear as hyperintensity surrounding the contrast-enhancing lesion (Leao et al., 2020; McKinnon et al., 2021). Neoplastic infiltration of GBM cells can also be assessed on T2/FLAIR images, as a characteristic feature is the blurring of the grey-white matter junction (Leao et al., 2020). On DWI, the solid enhancing component of the tumour often appears as increased signal due to diffusion restriction within areas of high cellularity, in comparison to surrounding vasogenic edema which typically has facilitated diffusion. The necrotic cavity often has facilitated diffusion as well; however, interpretation can be complicated if blood products are present (Young, 2007). High ADC values (low diffusion restriction) have also been shown to correlate with MGMT methylation status (Suh et al., 2018).

Oligodendrogliomas typically appear as round lesions and frequently show focal hemorrhage (Louis et al., 2016). Oligodendrogliomas are hypointense on T1w and only

about 50% of these tumours show enhancement on post-gadolinium images (Jenkinson et al., 2006). Figure 3b demonstrates an example of an oligodendroglioma with post-contrast enhancement on T1w imaging. On T2w images, vasogenic edema appears as hyperintense except for areas of calcification which are dark, due to signal loss (Van den Bent et al., 2008). Lastly, on DWI there is often no diffusion restriction, which can be a helpful in differentiating them from astrocytomas (Tozer et al., 2007).

The appearance of adult diffuse astrocytoma, IDH-mutant on MRI varies depending on grade. Typically, in grade 2 astrocytomas, on T1w image there is no (Fig.3d) or little enhancement (Fig. 3c), whereas solid areas of enhancement suggest a higher grade (Tervonen et al., 1992). Areas of necrosis on T1w post contrast imaging also signify a higher-grade astrocytoma (Louis et al., 2021). The "T2/FLAIR mismatch sign" is highly specific for diffuse astrocytoma, IDH-mutant, 1p/19q non-codeleted (Juratli et al., 2019). Tumours with this imaging sign are homogeneously T2 bright, with central signal suppression on FLAIR images (Figure 3c and 3d) (Juratli et al., 2019). This appearance is likely produced by cellular degeneration and edema, which is subsequently supressed on FLAIR imaging (Juratli et al., 2019; Watanabe et al., 1992). Lastly, on DWI, areas of low diffusion suggest a higher-grade, as decreasing ADC values correlate with increasing tumour grade (Hilario et al., 2012).

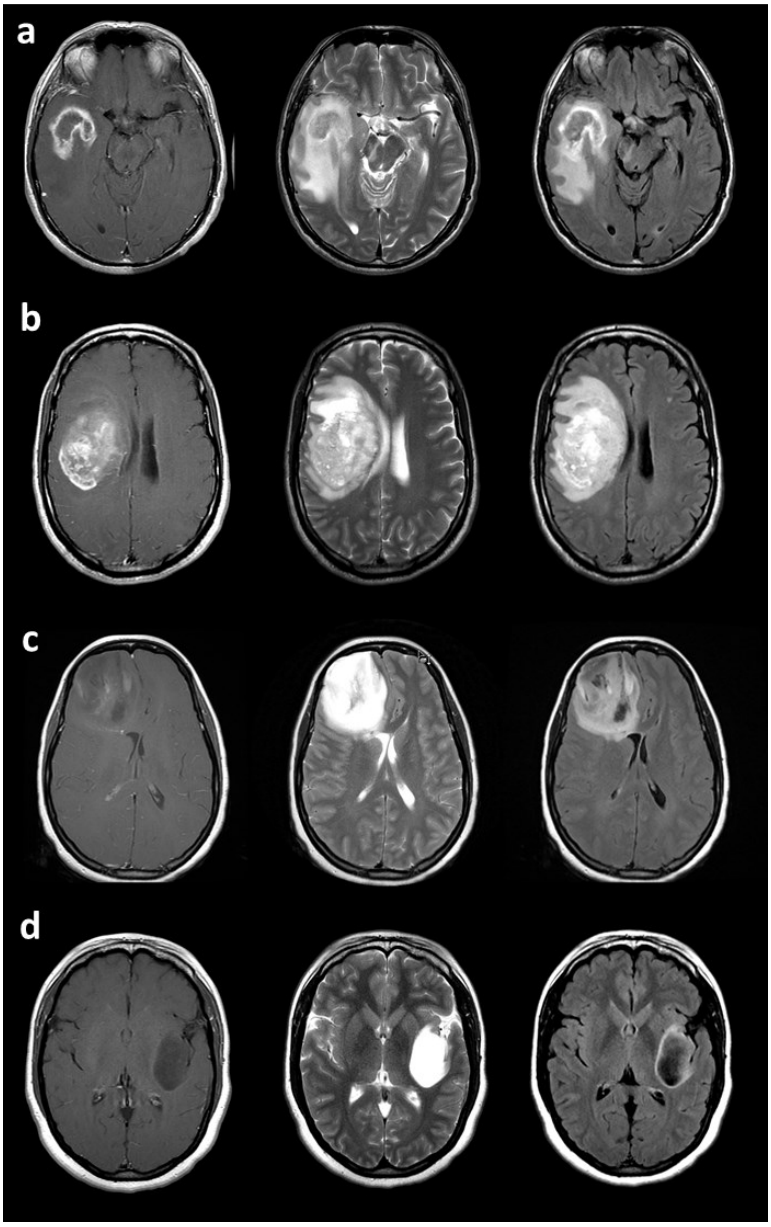

Figure 3. Adult diffuse gliomas on conventional MRI contrasts.
MRI contrasts are T1w post-gadolinium, T2w and T2 FLAIR from left to right. a) GBM, IDH wild-type, MGMT non-methylated. b) Oligodendroglioma, 1p/19q co-deleted, IDH-mutant and MGMT methylated. c and d) Diffuse grade 2 Astrocytoma, IDH-mutant and MGMT methylated showing T2/FLAIR mismatch.

1.2.2 Imaging Challenges of Post-treatment Glioma Assessment

With respect the assessment of tumour recurrence in high grade gliomas, conventional T1 weighted MRI is unreliable due to the subjective nature of image interpretation, further complicated by the similar appearance of treatment-related effects (Van Dijken et al., 2017). This is also true for the assessment of lower grade glioma transformation,

as patients undergoing chemoradiation to slow the tumour's progression also exhibit treatment-induced effects.

As a result of treatment induced vascular endothelial damage, there is increased permeability in radiated areas which causes increased contrast enhancement and can be mistaken for tumour recurrence (Hygino Da Cruz et al., 2011). This effect is known as pseudoprogression (PsP), in which new or growing enhancing lesions following the completion of chemoradiotherapy appear as progressive disease on T1w imaging, but subside on follow-up imaging without any change in treatment (Reimer et al., 2017). A similar issue occurs with T2w imaging in follow-up scans. Following surgical resection and chemoradiotherapy, treatment induced inflammation presents as T2/FLAIR hyperintensity (Leao et al., 2020). However, an increase in non-enhancing tissue (seen as T2 hyperintensity) could also signal disease progression, regardless of a stable appearance of contrast enhanced tissue (Chukwueke et al., 2019). Moreover, enhancement and edema on post-treatment imaging may demonstrate a mixture of treatment-related effects and viable tumour tissue, further complicating diagnosis (Hygino Da Cruz et al., 2011).

PsP typically occurs within 3-6 months following chemoradiotherapy and occurs in approximately 30-60% of patients that undergo concomitant chemoradiotherapy with TMZ (Dalesandro et al., 2016; Hygino Da Cruz et a., 2011). Furthermore, MGMT promotor methylated tumours have a significantly higher (91.3%) probability of PsP than unmethylated tumours (Lee et al., 2012; Reimer et al., 2017; Brandes et al., 2008).

Although PsP is typically clinically asymptomatic, some patients exhibit clinical deterioration (Hygino Da Cruz et al., 2011).

In addition to difficulties in diagnosing tumour recurrence, conventional MRI cannot reliably distinguish between low and high-grade gliomas (Van Dijken et al., 2017). The unreliability and subjectivity of MRI becomes a key issue in clinical decision-making and treatment planning (Reimer et al., 2017; Van Dijken et al., 2017). Identifying glioma grade early on is important for clinical decisions regarding the timing of treatment intervention (Leao et al., 2020). For post-treatment evaluation, if recurrence is missed, this may result in a delay of further intervention or stopping effective treatment. However, if treatment effects are mistaken as tumour recurrence, this may cause further damage to healthy tissue by unnecessarily continuing aggressive treatment (Leao et al., 2020). Decisions regarding secondary surgery also rely on timely diagnosis of tumour progression. Detecting tumour recurrence/progression quickly is crucial for survival outcomes; hence, reliable techniques to evaluate tumour behaviour are urgently needed.

1.2.3 Advanced MRI Techniques

Currently, the only way to differentiate between PsP and true disease progression is through follow-up imaging on conventional MRI; however, advanced MRI techniques are being examined as an alternative to overcome these issues. Advanced techniques such as DWI, perfusion weighted imaging and MR spectroscopy can be used to assess changes in cellular density, tumour-induced neovascularity and metabolite

concentrations, respectively (Van Dijken et al., 2017). In a meta-analysis of 35 studies, performed by Van Dijken et al. (2017), it was found that advanced MRI techniques showed a higher diagnostic accuracy in distinguishing between PsP and true progression than anatomical MRI, and that spectroscopy had the highest diagnostic accuracy among advanced MRI techniques.

Magnetic Resonance Spectroscopy (MRS) is a technique used to examine the chemical composition and biochemical changes of various tissues (Tolia et al., 2015). The resonance frequency of metabolites is measured in parts per million and plotted as peaks on a graph, which can then be used to compare normal brain tissue to abnormal tissue (Tolia et al., 2015). Gliomas typically have elevated choline and lipid levels, lactate peaks and lower N-acetyl aspartate levels (Hygino Da Cruz et al., 2011; Tolia et al., 2015; Seeger et al., 2013). Spectroscopy can depict structural degradation in cerebral tissue and detect metabolic changes associated with radiation injury before its appearance on imaging (Hygino Da Cruz et al., 2011). This could then be used to distinguish viable tumour tissue from PsP, with several studies identifying high choline/creatine ratio as the best predictor for recurrent glioma (Van Dijken et al., 2017; Seeger et al., 2013; Rabinov et al., 2002). However, distinguishing PsP from recurrence is still challenging, as PsP can have a similar spectroscopic profile to recurrent glioma because choline can also be elevated with PsP due to loss of neuronal function and cell membrane integrity (Hygino Da Cruz et al., 2011). Moreover, MRS has large voxels making it prone to partial volume effect (when a voxel contains a heterogeneous mix of tissue) which in turn makes it harder to detect changes in smaller lesions or heterogenous lesions (Young,

2007). MRS is also technically challenging, with long scan times making it susceptible to signal contamination (Van Dijken et al., 2017). Although there are promising results using MRS, there is no current consensus on threshold used among studies limiting the standardization of MRS for diagnostic decision-making (Young, 2007; Van Dijken et al., 2017).

Perfusion weighted imaging is an MRI contrast that allows relative cerebral blood volume (rCBV) and relative cerebral blood flow (rCBF) to be examined (Seeger et al., 2013). Perfusion weighted imaging can be performed using various techniques, including dynamic susceptibility contrast-enhanced imaging (DSC), dynamic contrast-enhanced T1w imaging (DCE), and arterial spin labelling (ASL). DSC is the most commonly used and straightforward technique for perfusion imaging, with readily available post-processing software (Essig et al., 2013). Studies using DSC imaging to assess differences in perfusion within a lesion have shown evidence of increased rCBV in recurrent glioma compared to stable disease (Seeger et al., 2013). In an analysis of 18 studies using DSC imaging, there was a pooled sensitivity of 87% and a specificity of 86% for differentiating between PsP and recurrence (Van Dijken et al., 2017). The disadvantages of DSC imaging include operator dependence, susceptibility artifacts and difficulties in rCBV quantification as values can vary over time and there is no consensus for optimum time point or threshold (Essig et al., 2013; Van Dijken et al., 2017). Steroids, which are commonly prescribed to post-operative glioma patients, are also known to influence DSC measures (Young, 2007). Moreover, rCBV may be less useful in differentiating PsP from early progressive disease in MGMT hypermethylated tumours.

(Dalesandro et al., 2016). Lastly, DSC has limitations in resolution, which decreases its capacity for anatomical and disease delineation (Seeger et al., 2013).

Analysis of five studies using DCE showed a slightly higher pooled sensitivity (92%) than DSC, with a specificity of 85% (Van Dijken et al., 2017). Although DCE had the highest accuracy for distinguishing PsP from recurrence among perfusion techniques, DCE is not widely used due to the complexity of image acquisition and post-processing software (Essig et al., 2013). Lastly, ASL can be used for perfusion weighted imaging without the administration of a contrast agent, by using magnetically labelled blood as an endogenous tracer to measure rCBF (Essig et al., 2013). Although ASL offers the advantage of being completely non-invasive, the technique is not universally available and there is scarce evidence of its use for distinguishing between PsP and recurrence (Van Dijken et al., 2017).

The third commonly studied advanced MRI technique for assessing glioma progression, transformation and recurrence is DWI. ADC measurements from DWI have been studied for the assessment of gliomas, as the heterogeneity of the tumour tissue leads to variations in diffusion restriction (Werner et al., 2019). Pathologic processes such as the degradation of cellular integrity within necrotic regions leads to areas with increased ADC values relative to normal tissue (Lee et al., 2012). On the other hand, solid tumour components reflect lower ADC values and could be used to assess regions of rapid cell proliferation congruent with tumour growth and progression (Lee et al., 2012). Despite ongoing research on ADC predictive value for differentiation between tumour recurrence and PsP, evidence is scarce and often conflicting (Kwee et al., 2010). In the

meta-analysis performed by Van Dijken et al. (2017), ADC values had the lowest diagnostic accuracy and should be combined with other advanced techniques. The low accuracy of ADC could be a result of heterogeneous signal intensities, which could be cellular tumour or inflammatory processes and is, again, compounded by the lack of standardized cut-off points for diagnostic decision-making (Hygino Da Cruz et al., 2011).

1.3 Interest in Circulating Biomarkers for Adult Gliomas

Novel approaches are urgently needed to assess progression and transformation, and to detect recurrence of gliomas after treatment with greater confidence. Monitoring patients with low-grade gliomas and patients with treated gliomas requires a quick and reliable test that can be obtained repeatedly and noninvasively. One promising approach is to examine molecular markers through a simple venous blood sample, termed “liquid biopsy” (Doyle & Wang, 2019). Liquid biopsy is a minimally-invasive technique that is currently being studied for its ability to test for tumour-derived biomarkers such as extra-cellular vesicles (EVs) (Osti et al., 2019; Doyle & Wang, 2019; Rooj et al., 2016).

EVs are small membrane-bound vesicles that do not contain a nucleus and are released by all cells as a means for intercellular communication (Yekula et al., 2019). EVs are subdivided into three main categories: exosomes, microvesicles and apoptotic bodies, which differ in size, cargo, function and biogenesis (Doyle & Wang, 2019). EVs have been shown to contain various cargo, such as small RNA (sRNA) and proteins, that mimic its donor cell’s physiology and could be used to determine their cells of origin (Simon et al.,

2020). EVs are secreted by all cells, including neoplastic cells of gliomas, in which case they could reflect tumour behaviour (Osti et al., 2019; Balakrishnan et al., 2020).

EVs that are released from neoplastic cells are thought to play a critical role in establishing progression (Osti et al., 2019). Recent studies have demonstrated the multifaceted roles of EVs in transforming the glioma microenvironment into a tumour promoting niche, in which normal cell-derived EVs are co-opted to facilitate tumour invasion (Osti et al., 2019; Yekula et al., 2019). EVs are known to modulate tumour proliferation, induce angiogenesis, reprogram metabolic activity, evade immune response and lead to drug resistance (Czernek & Düchler, 2017; Yekula et al., 2019). Glioma-derived EVs that are shed into the tumour microenvironment end up circulating in the bloodstream due to BBB compromise (Balakrishnan et al., 2020).

Liquid biopsy can detect EVs shed into the blood stream by gliomas, offering a complementary approach to tumour surveillance (Balakrishnan et al., 2020; Doyle & Wang, 2019). Currently, tissue biopsy is used to determine the molecular profile of gliomas; however, it is both invasive and prone to sampling bias (Saenz-Antoñanzas et al., 2019). Liquid biopsy could potentially offer an alternative to invasive tissue biopsy, as it contains information from the entire tumour which enables confirmation of the tumours molecular profile (Saenz-Antoñanzas et al., 2019; Siravegna et al., 2019). Tissue biopsy is performed during surgical resection; however, not all glioma patients are candidates for surgical resection due to inaccessible lesions or surgical co-morbidities (Balakrishnan et al., 2020). Moreover, re-biopsy after initial resection is an unfavourable option for distinguishing PsP from recurrence as it is very invasive. Liquid biopsy would

enable clinicians to bypass an invasive tissue biopsy in patients that are poor surgical candidates and allow regular monitoring throughout treatment (Doyle & Wang, 2019).

1.3.1 Extracellular Vesicles in Clinical Research

A common interest in EV research is studying their correlation to disease state, especially with regard to their prognostic, diagnostic and predictive biomarker abilities in glioma patients (Tankov & Walker, 2021). It has been shown that RNA profiles of glioma secreted EVs are unique to glioma cells and therefore glioma-derived EVs can be distinguished and isolated from other circulating EVs (Simon et al., 2020). Some studies have also suggested that tumour cells release greater quantities of EVs than healthy cells, although this is still under debate (Osti et al., 2019; Xavier et al., 2020). Therefore, clinical research has primarily focused on RNA and protein profiling of EV cargo as well as assessing overall EV concentration throughout the disease timeline (Simon et al., 2020; Osti et al., 2019).

With regards to EV concentration specifically, it has been calculated that a single GBM cell is capable of producing 10,000 EVs within 48 hours *in vitro*, and that EVs have a half-life of approximately 5 hours *in vivo* (Skog et al., 2008; Rank et al., 2011). In a recent study performed by Osti et al. (2019), it was found that GBM patients demonstrated higher EV concentrations in their peripheral blood than healthy patients and that this concentration drops following surgical resection of the tumour. EV concentration was also correlated with the progression of high-grade astrocytoma patients and a correlation between higher amounts of necrosis and lower EV concentration was also

noted (Osti et al., 2019). This could indicate that EV concentrations are tumour volume dependent; however, other factors such as tumour cellularity and level of perfusion may be at play.

The molecular profiling of EV cargo has also revealed promising biomarkers for determining glioma classification and grade and is being studied for proteomic signatures of tumour invasiveness and aggression (Santangelo et al., 2018; Hallal et al., 2019; Skog et al., 2008). Santangelo et al. (2018), found that concentrations of micro-RNA (a subset of small RNA) within EVs (specifically miR-21, miR-222 and miR124-3pm), were grade dependent in astrocytoma patients, highlighting those levels of small RNA (sRNA) could be used to predict tumour grade. (Hallal et al., 2019), demonstrated that IDH wild-type and IDH mutant gliomas also have distinct sRNA signatures, adding to the increasing evidence that the molecular profile of EVs captured from peripheral liquid biopsy is consistent with tissue biopsy information.

Although there is strong evidence of a correlation between liquid biopsy and tissue biopsy, currently, it is not known how liquid biopsy correlates MRI surveillance imaging. There is little evidence regarding the correlation between EV concentration and features of tumour progression and recurrence on MRI.

1.3.2 The Halifax Cohort

To study the utility of glioma-derived EVs as a biomarker of tumour behaviour, adult patients treated for a glioma at the Queen Elizabeth Health Sciences Centre are recruited for participation in a longitudinal cohort study. Blood samples are taken

following an initial diagnostic MRI, at the time of surgery or tissue biopsy, and in conjunction with all follow-up standard-of-care imaging. Plasma is extracted by the Weeks Lab and is sent to the Atlantic Cancer Research Institute (ACRI) in Moncton, New Brunswick. The ACRI uses a patented technology, called Vn96, to isolate and quantify EVs and to perform sRNA profiling. Tumour-specific EV counts can then be correlated with the course of disease and changes seen on clinical MRI.

1.4 Image-based Monitoring of Adult Gliomas in Clinical Trials

The current standard for MRI monitoring of brain tumours in clinical trials relies on the Response Assessment in Neuro-Oncology (RANO) criteria (Chukwueke et al., 2019; Leao et al., 2020). For the measurement and quantification of brain tumour components, under the RANO criteria, there is measurable and non-measurable disease. Measurable disease is described as enhancing lesions with clearly defined margins and 2 perpendicular dimensions that are both $\geq$10mm, not including a necrotic core or a resection cavity (Figure 4) (Leao et al., 2020). Non-measurable disease includes any non-enhancing tissue, lesions less than 10mm in diameter and lesions with ill-defined margins (Leao et al., 2020). RANO uses bi-dimensional linear measurements as a surrogate for tumour volume. These measurements are performed on up to 5 enhancing foci, which are then added together for the final measurement.

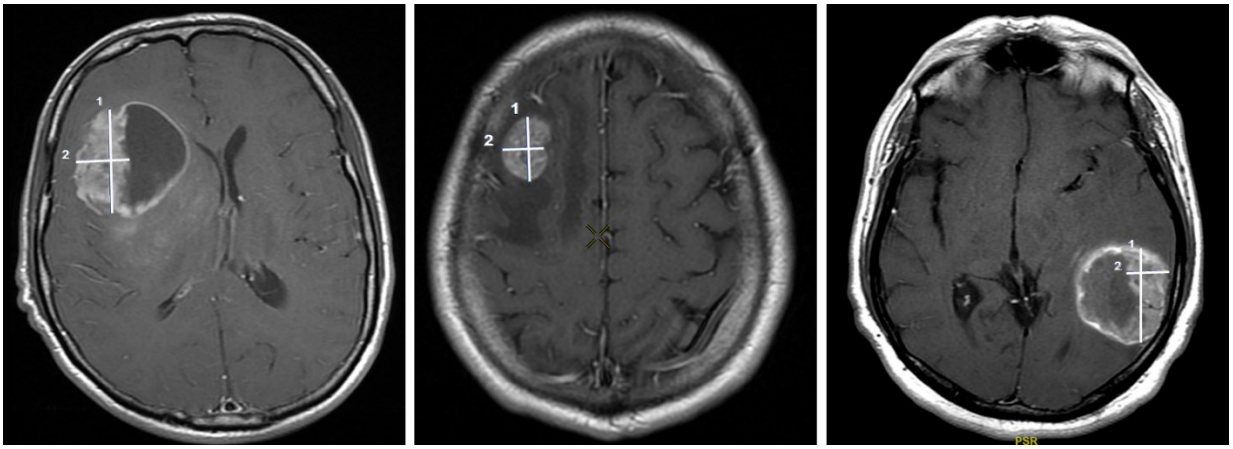

Figure 4. Measurable lesions with bi-dimensional measurements according to RANO criteria.
Only enhancing nodular components with defined margins and diameters ≥10mm are measured. Surgical cavities or cystic and necrotic components are excluded. Patient MRIs are WWS06A, WWS09A, and WWS35A from left to right.

Although the standardization of brain tumour measurements is important for reproducibility and clinical management decisions, there are several practical issues with the RANO criteria. For the measurement of the enhancing tumour component, lesions with a central necrotic component or an irregular enhancing thick wall are subject to great measurement variability (Yang et al., 2014). Differences in measurement technique, such as exclusively measuring the enhancing component or measuring the entire lesion, lead to varying results and presents a considerable challenge for quantification.

Secondly, under the RANO criteria, post-resection examinations cannot be assessed reliably, as they contain surgical cavities which are considered non-measurable (Fig. 5c). This poses issues for the accurate quantification of the extent of a surgical resection, which is known to be a significant prognostic indicator for progression free survival in glioma patients (Lacroix et al., 2001). A similar issue arises when attempting to quantify

the volume of peritumoural edema as well as non-enhancing T2w hyperintense solid tissue, as non-measurable disease also includes T2/FLAIR hyperintense tissue (Fig. 5f). Peritumoural edema is a common feature of gliomas and the lack of a standardized method for the reproducible quantification of glioma related edema may be a contributor to the ongoing debate over its prognostic implications (Schoenegger et al., 2009; Lacroix et al., 2001). Moreover, astrocytomas with a T2/FLAIR mismatch sign become difficult to measure, as they often show very little or no enhancement and are predominantly examined on T2/FLAIR MRI contrasts (Fig. 5e) (Juratli et al., 2019).

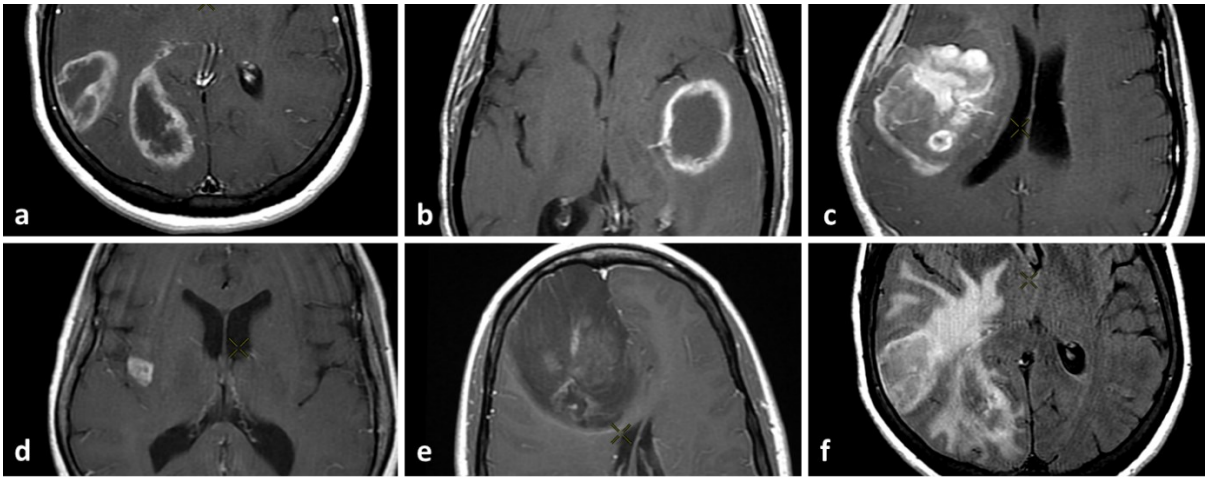

Figure 5. Non-measurable disease under the RANO criteria.
Lesions with central necrotic or cystic cavities (a, WWS07A; and b, WWS27A). Lesions with surgical cavities (c, WWS04B) or bi-dimensional diameters <10mm (d, WWS26A). Disease with ill-defined margins (c and e, WWS32A) as well as T2/FLAIR hyperintense non-enhancing lesions (f, WWS07A) are also characterized as non-measurable.

To assess measurable and non-measurable disease objectively, as well as incorporate clinical factors, the RANO criteria suggest 4 categories of response: complete response, partial response, stable disease and progressive disease (Leao et al., 2020). These criteria utilize large percent-based increases or decreases in the measurable enhancing

lesions, rely on visual assessment of non-measurable disease, account for changes in clinical evaluations and steroid use, and are considered on a 4-week timeline (Leao et al., 2020). The disadvantages of using these 4 categories for assessment is that standard-of care MRI is typically performed every 3 months rather than 4 weeks, small changes in enhancing lesions that could reflect progression/recurrence would be overlooked or miscategorized and visual assessment of non-enhancing lesions is subjective in nature (Yang, 2014). Although the RANO criteria offers standardization, a surrogate for tumour bulk it is not ideal for clinical correlations with physiological parameters such as EV shedding or RNA profiles. For these, a volumetric technique would be better a priori.

1.4.1 Tumour Volumetry and Segmentation Techniques on MRI

In order to address the pitfalls of the RANO criteria, a number of methods exist for brain tumour quantification. Brain tumour segmentation on MRI is an increasingly popular area of research, which consists of extracting various tumour tissues, such as contrast-enhancing tissue, peritumoural edema and necrosis, from normal brain tissue (Wadhwa et al., 2019). Segmentation techniques are advanced processes for the volumetric analysis of brain tumour tissues and fall under three categories: manual, semi-automatic and automatic (Wadhwa et al., 2019). Segmentation on MRI can further be classified as threshold-based, boundary-based and region-based, which are the most predominant within the literature, however, other technique classifications include pixel-based and model-based segmentation (Wadhwa et al., 2019).

Fully-automated techniques have utilized machine learning algorithms for segmentation of gliomas and shown good accuracy for both low- and high-grade gliomas (Van Kempen et al., 2021). According to the Multimodal Brain Tumor Image Segmentation Benchmark (BRATS) 2015, many algorithms for automated segmentation show similar variability to trained human raters for different sub-regions, but not one technique showed high accuracy for all sub-regions (Menze et al., 2015). The development of automated segmentation methods is technically challenging, as differentiation of diseased tissue relies on the intensity differences from normal brain matter (Menze et al., 2015). Techniques that have shown promising results, such as Brain Tumour Image Analysis (BraTumIA) (Porz et al., 2014), are often designed to work primarily on pre-operative MRIs, leaving a gap in post-operative tumour assessment and quantification. Moreover, fully-automated techniques limit or do not allow user intervention, making it difficult to remove misclassified non-tumour tissue from the final product (Menze et al., 2015).

Semi-automatic segmentation techniques offer the advantage of user interaction in either initialization or post-processing, and are considered beneficial within a clinical workflow setting (Gering et al., 2020; Menze et al., 2015). Among semi-automated algorithms, computation times vary from a few minutes to several hours, with a trade-off between speed and segmentation quality (Menze et al., 2015) Algorithms with simple user initialization proposed by Guo (2013) and Hamamci (2012) discussed in the BRATS 2015, have demonstrated good results for 2D contour-based segmentation and whole tumour segmentation respectively, and exhibited fast processing times (Menze et al., 2015; Hamamci et al., 2012). Semi-automated techniques have been shown to

outperform fully-automated methods; however, complex post-processing algorithms limit their adoption into research and clinical practice (Pooja et al., 2021).

Due to the varied and heterogeneous nature of gliomas, not one technique or automated process can account for their diversity. Segmentation is difficult due to limitations of poor spatial resolution, low contrast, ill-defined boundaries, inhomogeneity, partial volume effect, noise, variability of tumour shapes and acquisition artifacts (Wadhwa et al., 2019). A meta-analysis of currently available segmentation techniques cited semi-automated techniques with little user intervention as more acceptable for clinical use, yet deemed manual segmentation by a trained rater as the ground truth (Wadhwa et al., 2019).

Manual segmentation by a trained rater with anatomical and morphological knowledge of gliomas is used for the comparison of semi-automated and fully-automated techniques and is considered to be the best method a priori (Wadhwa et al., 2019). A drawback of manual segmentation is that results are subject to intra- and inter-observer variability since it relies on the knowledge of the observer and requires expertise in the field (Pooja et al., 2021). Manual segmentation techniques often utilize 2D free-hand contour-based segmentation making them time-consuming and inefficient for assessing whole tumour volume (Menze et al., 2015).

Currently, no segmentation technique is widely used or universally accepted as standard. It is essential for techniques of tumour volumetry to be accessible and efficient for their implementation into practice and clinical research. Furthermore, there

is little research on whole-tumour segmentation techniques for advanced MRI contrasts such as DWI or Perfusion weighted imaging. Whole-tumour volumetry is of crucial importance for diagnosis, monitoring disease progression and treatment response; thus, a reliable method that quantifies multiple tumour parameters on several MRI contrasts and can be used on readily available clinical software is urgently needed.

1.4.2 Evaluation of DWI

Segmentation techniques have largely focused on quantifying tumour components on conventional MRI contrasts; however, few are applicable to advanced MRI contrasts such as DWI (Wadhwa et al., 2019). Evaluation of DWI typically uses minimum ADC values as a biomarker for malignancy, and this is typically assessed by sampling within the enhancing portion of the tumour (Kono et al., 2001; Darbar et al., 2018). However, sampling issues arise when defining a specific point within the tumour as a region of interest (ROI) instead of assessing the tumour tissue as a whole. The ROI approach is a major limitation of studies evaluating diffusion restriction, as gliomas are known to be extremely heterogeneous and a single point measure neglects the variation between different regions of the tumour tissue (Reimer et al., 2017). The use of point ROIs is subjective and may bias areas high diffusion restriction instead of taking into account the level of restriction within the entire tumour boundary. Secondly, this compounds the issue of partial volume effect, especially when examining cases of PsP vs. recurrence, as there is often a mix of radiation necrosis and viable tumour tissue throughout the restricted area (Reimer et al., 2017). ADC values are also seldom examined within non-enhancing tumour tissue, despite this being acknowledged as an

area of diseased tissue (Kono et al., 2001). This highlights the need to examine ADC values across the whole tumour.

A study that analyzed ADC values within both enhancing and non-enhancing tissue, found that GBM patients had lower ADC values (820 x 10^{-6} mms^2/s) than grade 2 astrocytomas (1.14 x 10^{-3} mms^2/s) within the enhancing portion, but showed no significant difference between ADC values within the peritumoural T2 hyperintense region (Kono et al., 2001). Several different mean ADC values and cut-off points for analysis have been suggested for differentiating between tumour grades as well as radiation necrosis and recurrent tumour (Darbar et al., 2018; Orlandi et al., 2016; Lee et al., 2012). Darbar et al. (2018) also noted high grade gliomas to be 0.363-0.727 $\mu m^2/s$, but used an 0.8 $\mu m^2/s$ high cut-off for analysis. In contrast, Orlandi et al. (2016) suggested a low cut-off of 0.5 and high cut-off of 1.5 ($\mu m^2/s$) by using ADC histogram plots. Additionally, Lee et al. (2012) suggested an ADC cut off of 1.2 $\mu m^2/s$ to differentiate between PsP and true progression. In each of these studies, the objective was to assess the mean ADC within an area of highly restricted tissue, which is a likely source of the variation between studies and lack of a standard cut-off point. A better approach might be to measure the volume of tissue at incremental levels of restriction in order to assess how much of the tumour is restricted. Moreover, the volumes of restricted tumour tissue should be measured within both the enhancing and non-enhancing tumour components.

1.5 Objectives

In order to address the shortcomings of RANO measurements and address the gap in segmentation and volumetry for advanced MRI contrasts, I have developed a protocol for manual segmentation using readily available clinical software. The protocol for segmentation and quantification of tumour tissue utilizes locally available tools that are already embedded within the clinical workflow, but are not currently used to extract volumetric information. The segmentation technique needed to be able to: 1) determine volume of contrast-enhancing tissue, 2) determine the gross total tumour volume (enhancing, non-enhancing and vasogenic edema), 3) determine the volume of diffusion-restricted tumour tissue at multiple thresholds within boundaries defined by (1) and (2). The technique had to be applicable to scans obtained at the time of diagnosis and to serial scans obtained following treatment.

The specific objectives of the thesis were: 1) to develop a technique for volumetric assessment of each of the above MRI-based tumour features, using readily available clinical post-processing software, 2) assess the intra- and inter-rater reliability of the technique, 3) demonstrate the use of the technique to track MRI-based tumour features longitudinally in participants from the Halifax cohort, and 4) begin to assess the correlation between MRI-based tumour features and biomarkers obtained by liquid biopsy as these become available.

CHAPTER 2 RESEARCH METHODS

2.1 Participants

Adult patients undergoing treatment for a grade 2-4 glioma, following an initial diagnostic MRI at the Queen Elizabeth II (QE2) Health Science Centre, were identified by a tumour nurse practitioner. Patients with a with Karnofsky Performance Scores (KPS) >70 were invited to participate in the study. Patients provided informed consent for liquid biopsy and for the retrospective analysis of their serial standard-of-care MRI examinations. MRIs were performed 48 hours following surgery and longitudinally throughout chemoradiotherapy. Blood was drawn prior to surgery, during surgery/biopsy, 2 weeks after surgery and within a 48-hour window of all follow-up standard-of-care MRIs.

High grade glioma patients received standard concurrent radiation and chemotherapy using TMZ for 28 days. Adjuvant chemotherapy was administered for six to twelve 28-day cycles. Patients with lower grade gliomas were followed with MRI, and liquid biopsy was performed every 6 weeks until malignant transformation was identified by imaging (Fig. 6). Imaging was also obtained if patients showed signs of neurological deterioration.

This study was an observational prospective sub-study of a larger clinical cohort study and was approved by the Nova Scotia Health Authority Research Ethics Board. Within this sub-study, 40 total patients were enrolled and of these, 34 patients were examined for MRI features. A total of 9 patients had pre-operative EV counts available and a total

of 10 patients had RNA data for post-treatment examinations (25 exams in total). Patients were excluded from further study if the final diagnosis was not that of an adult diffuse glioma (n=4), standard imaging protocol was not followed (n=1) or if the patient had a previous resection for a brain tumour (n=1). Diagnostic MRI examinations were also excluded from analysis (n=4) if a more recent pre-operative MRI was available. For the purpose of this study, grade 4 astrocytomas were considered as GBM diagnosis under the WHO CNS4 classification system (Louis et al., 2016) which was in place at the commencement of this study. Patient details are summarized in Appendix B, Table 5.

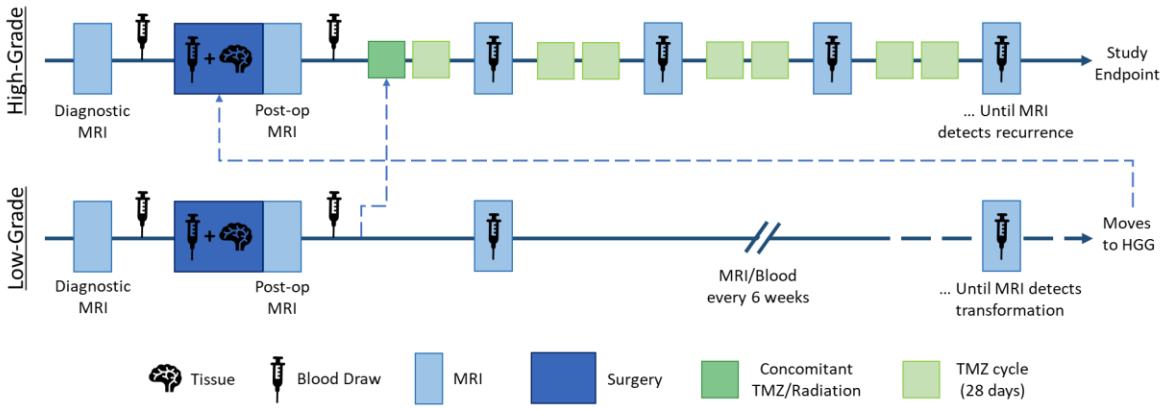

Figure 6. Timeline of study procedures.
Low grade glioma patients either move into chemo-radiotherapeutic regimen following surgery or are monitored until imaging detects transformation. All radiation and chemotherapy cycles are 28 days.

2.2 Magnetic Resonance Imaging

All MRI examinations were obtained with a 1.5 Tesla GE scanner (Signa HDx, GE Healthcare, Waukesha, WI) with an 8-channel, high resolution, phased array head coil. Imaging protocol include the following sequences in order: 3 Plane localizer SSFSE, Sagittal T1 FLAIR, Axial T2 PROPELLER, Axial DWI, Axial T1 FSE, Axial T2 FLAIR with

contrast (CE), Axial T1 FSE +CE, Coronal T1 FSE +CE. The imaging parameters of the 6 contrasts examined in this study are described in detail below.

2.2.1 T2w and FLAIR Imaging

T2w imaging was performed using a PROPELLER sequence to reduce patient motion. Imaging parameters for scan and acquisition timing were TR 6250 ms, TE 84 ms, ETL 26, FA 111^{o} and NEX 2. The scan range parameters were field of view (FOV) 220 x 220 mm^2, matrix 320 x 320, and slice thickness 5mm. T2 FLAIR imaging was obtained after gadolinium enhancement and the following imaging parameters: TR 9000ms, TE 124ms, TI 2000, ETL 30, FA 160^{o}, NEX 1, FOV 220 x 220 mm^2, matrix 256 x 224 and slice thickness 5mm.

2.2.2 DWI Imaging

DWI was performed using a spin echo pulse sequence with the following imaging parameters: TR 8000ms, TE 73.9 ms, FA 60^{o}, NEX 1, FOV 220 x 220 mm^2, matrix 160 x 192 and slice thickness 5.8mm. ADC maps were created using b = 0 and b= 1000 mm^2/s.

2.2.3 T1w Imaging

T1w imaging was acquired using an FSE-XL pulse sequence optimized to GE scanner for blurring cancellation. Imaging parameters were TR 562 ms, TE 25.6 ms, ETL 3, FA 111^{o}, NEX 2, FOV 220 x 220 mm^2, matrix 320 x 192 and slice thickness 5mm. Axial T1w CE imaging was acquired using the same imaging parameters with the addition of a gadolinium contrast agent.

2.2.4 Perfusion Imaging

Perfusion weighted imaging was acquired using a gradient echo sequence with phase correction and contrast. Imaging parameters were TR 2275 ms, TE 45 ms, FA 60^{o}, NEX 1, FOV 240 x 240 mm^2, matrix 96 x 96 and slice thickness of 5mm.

2.3 Image Post-processing

MRIs were taken from PACS archive and anonymized, then given a study code (e.g., WWS01) according to time point. Pre-operative MRIs were labelled as "A" scans (WWS01A) and post-operative MRIs were labelled as "B" (WWS01B). Follow-up MRIs were taken approximately every 3 months and labelled as C, D, E, etc. until study endpoint for the patient. The anonymized MRIs were stored on the AW 3.2 server and imported into ReadyView^{TM} (GE Healthcare, Chicago, IL) for post-processing and analysis. Volumetric analysis of serial MRI examinations was performed using segmentation and thresholding tools embedded in the ReadyView^{TM} software.

Three MRI features of tumour components were examined and quantified: 1) gadolinium enhancement in T1w images, 2) T2 FLAIR hyperintensity and 3) ADC values from Diffusion Weighted MRI. All images were pre-processed for motion correction. The method used for segmentation was a blend of manual segmentation of tumour boundaries and threshold-based segmentation. Although intensity-based thresholding provided a semi-automated step in removing non-tumour tissue, the threshold was manually set according to patient specific tumour signal intensity. Moreover, user intervention was available at each step throughout the protocol, prior or following the

intensity thresholding step. Segmentation was performed on T1w and T2 FLAIR images. The net enhancing volume and net FLAIR hyperintense volume were defined as regions of interest (ROIs) and cloned to ADC maps for analysis of diffusion restriction within the gross tumour volume and within the enhancing tumour component. Although this sub-study did not examine perfusion imaging, the technique developed can also be applied to perfusion images with parametric maps of relative cerebral blood flow (rCBF) and relative cerebral blood volume (rCBV) using ROI cloning, which can be seen in Appendix A.

Cystic tissues were removed from volumetric analysis in all three parameters. Necrotic tissue was also excluded from measurement using patient specific intensity thresholding. Lastly, T1 bright lesions on pre-gadolinium scans, such as hematomas, were removed using segmentation and ROI cloning followed by reverse object removal.

2.3.1 Removing pre-gadolinium T1 hyperintensity from exam series

Anonymized MRIs on the AW server were imported into Readyview^{TM} and analyzed within the "ADC Volume Viewer". A 3-pane split view was used throughout the segmentation process in order to examine contrasts consecutively and with the aid of a reference image. Pre-processing for motion correction was applied before analysis. First, the pre-gadolinium T1 FSE scan was visually analyzed for areas of T1 hyperintensity. If there was no evidence of T1 pre-contrast hyperintense lesions, post-processing proceeded to segmentation of the gadolinium-enhancing tumour tissue described in the following section (2.3.3).

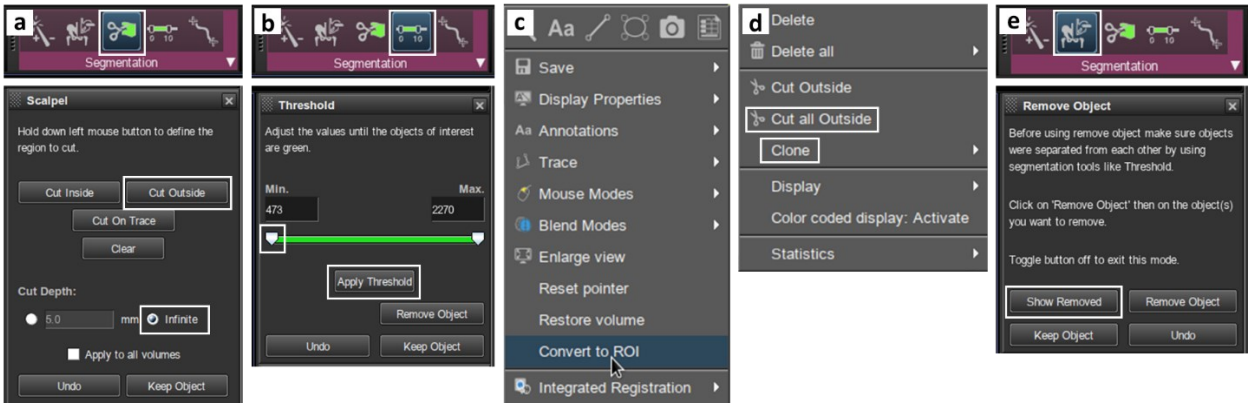

Figure 7. Tools embedded within ReadyView™ software used for post-processing. a) *Scalpel* tool used for freehand segmentation of tissue, with cut-outside or cut-inside options on infinite or dynamic cut depths (mm). b) *Threshold* tool used for patient-specific intensity-based thresholding, with slider bar and visual shading (green) of included areas within the chosen threshold. c) Post-processing options, including *convert to ROI*, used for define regions of interest in 2D planes. d) ROI processing options, including *Clone*, used for cloning ROI to other exams within the series; and *Cut all outside*, used for removing tissue outside of defined ROIs. e) *Remove object* tool used for "reverse ROI removal" by choosing *Show removed* to display background and remove tissue within defined ROIs.

In the axial plane, the largest section of a T1w bright lesion was loosely encircled using the Scalpel tool (Fig. 7a) with cut depth set to infinite, ensuring all lesion boundaries were included within the segmented area (Fig. 8b). The background was then removed using *Cut all outside*, with the circled area of hyperintensity remaining. The exam was then switched into the coronal plane and the largest section of hyperintensity was again crudely segmented (Fig. 8c). Exam view was subsequently switched into 3D while keeping a second axial T1w reference image juxtaposed. In 3D view, any anatomical T1 bright structures, such as the inner table of the skull or scalp fat, remaining in the field of interest were removed using the Scalpel tool (Fig. 8d). Intensity-based thresholding (Fig. 7b) was then applied to the remaining volume to remove intermediate-signal intensity tissues such as white and grey matter surrounding the lesion. The cut-off value

used for thresholding was patient-specific in order to meet the boundaries of the hyperintense lesion (Fig. 8e) to generate the final segmented product (Fig. 8f).

The final product of T1 hyperintensity was then switched from 3D view into axial view and the area was defined as an ROI (Fig. 8g). This ROI was then cloned (Fig. 7d) to all exams within the series (Fig. 8h). The background was then removed from T1w post-gadolinium and T2 FLAIR images by using *Cut all outside* function (Fig. 7d). Using the object removal tool (Fig. 7e), the *Show all removed* feature allowed the image to be reversed. This reversed image would now have the pre-gadolinium T1 hyperintensity removed for further analysis on T1w post-gadolinium and T2 FLAIR images (Fig. 8i).

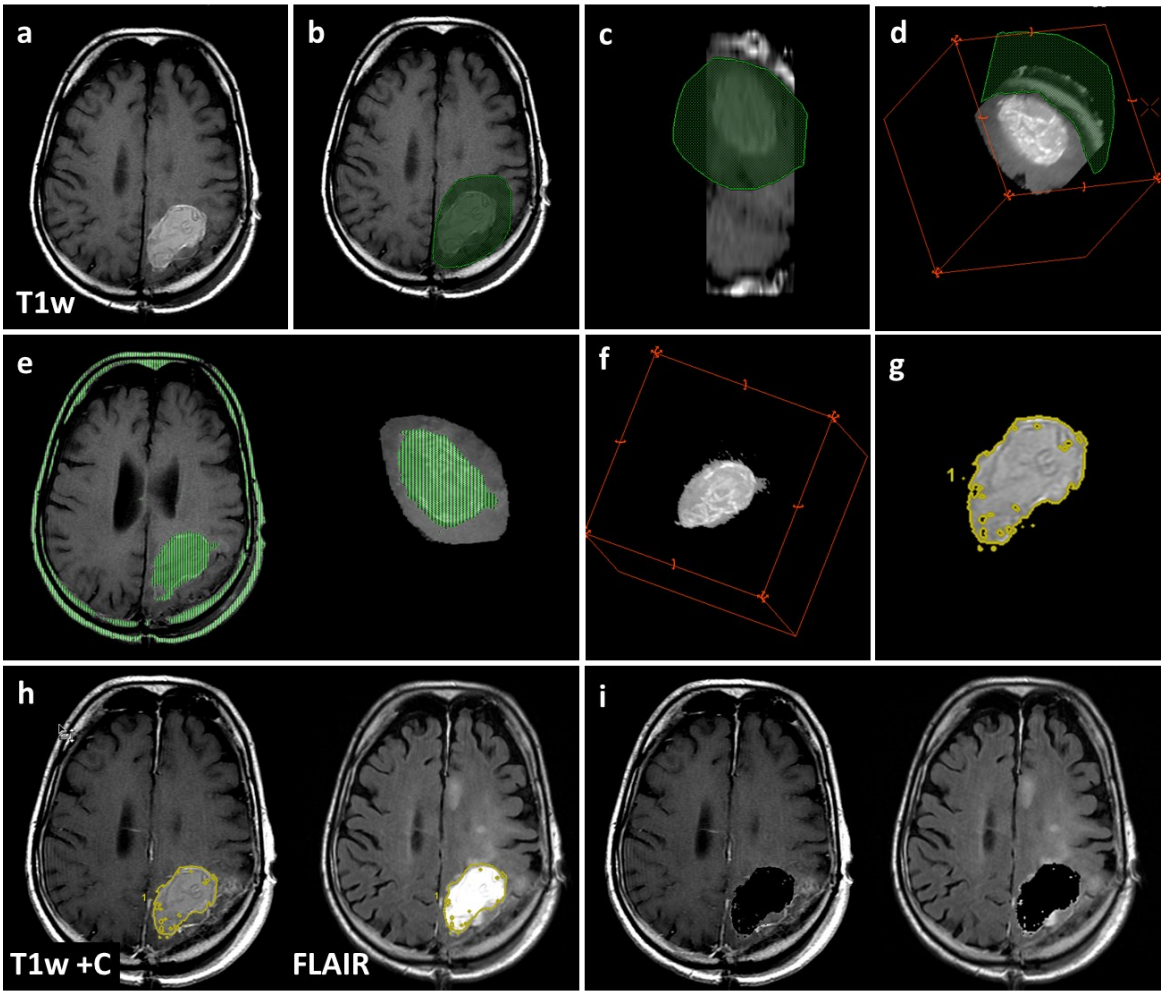

Figure 8. T1w pre-gadolinium hyperintensity exclusion.
a) T1w image of WWS25B (post-operative exam) showing fluid filled cavity. b) Crude segmentation of axial plane. c) Crude segmentation on coronal plane. d) 3D rendering following bi-planar segmentation, further segmented for non-tumour tissue that is T1 bright. e) Intensity-based thresholding of segmented product. f) Final product of pre-gadolinium T1 bright lesion in 3D view. g) Final product set as ROI in axial view. h) ROI cloned to T1w post-gadolinium and T2 FLAIR exams. i) ROI removed from exams using reverse object removal, any remaining enhancement/hyperintensity is measured from these images.

2.3.2 Volume of gadolinium-enhancing tumour tissue

MRIs pre-processed for T1w hyperintensity due to hematoma or surgical cavities, as well as MRIs without any evident T1w hyperintensity were used for measuring volumes of gadolinium-enhanced tumour tissue. Following a similar step-wise process as described earlier, bi-dimensional segmentations were performed on axial and coronal planes to produce a crude volume for further segmentation in 3D view (Fig. 9a-d). Once all non-tumour T1 bright tissue was removed, the tissue was thresholded according to the enhancing boundaries of the tumour and defined as an ROI for quantification and future use on ADC maps (Fig. 9e-g), named the contrast-enhanced (CE) ROI. The measurement could be taken by using the volume measurement tool in Readyview, which permits quantification of the remaining tissue in the exam, or by setting the tissue as an ROI, both recorded in cm^3 of enhancing tumour tissue.

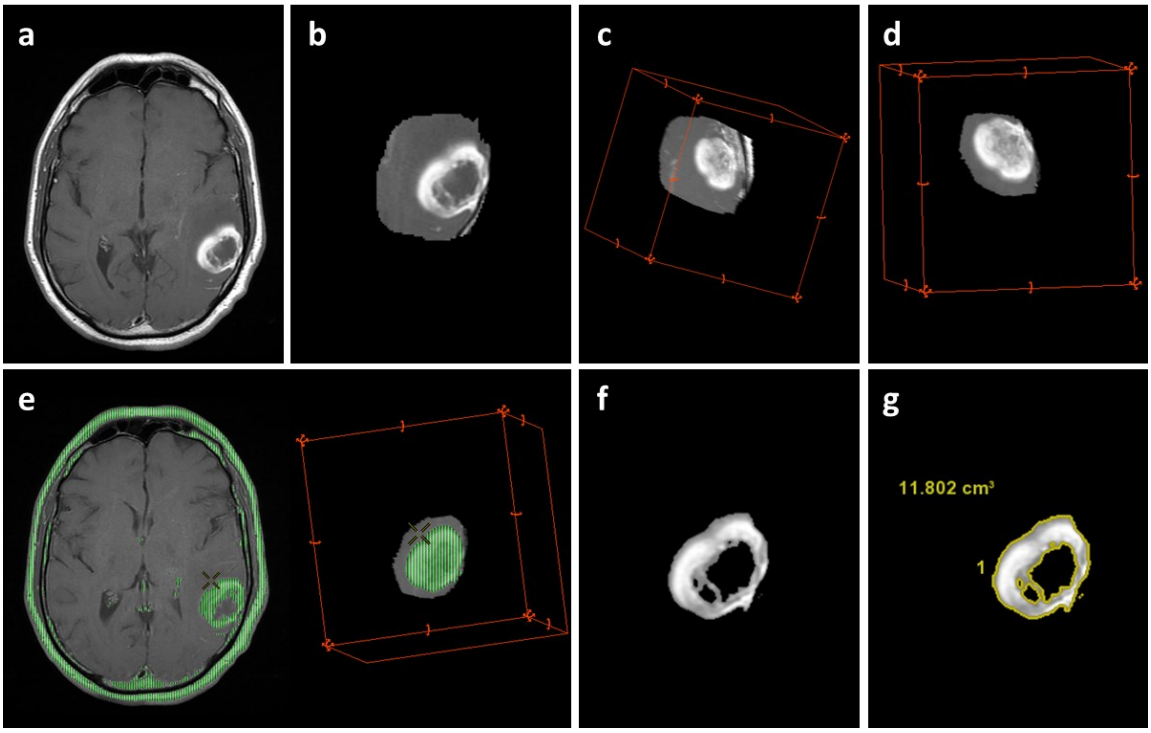

Figure 9. Segmentation of the CE component of a GBM on T1w imaging.
a) Contrast enhanced T1w image of WWS38A. b) Rough segmentation on axial plane followed by a segmentation on the coronal plane. c) 3D rendering of the contrast enhancing component following double segmentation on axial and coronal planes. d) 3D rendering following segmentation of non-tumour tissue that is T1 bright. e) Intensity thresholding of the 3D enhancing tissue with axial 2D reference image. f) Final product of the contrast enhancing component in axial view following thresholding. g) Enhancing tissue set as ROI and measured in cm^3.

Each measurement was taken 3 times (including any pre-processing steps to remove T1 bright tissue), separated by a minimum of 1 week between measurements. Quantification of the volume was only completed as the final step in the technique and could not be altered once taken. Triplicate measurements of the first 6 patients at baseline (WWS01A-06A) were taken by a trained observer (Willms, M.) and by an experienced neuroradiologist (Schmidt, M.), and used to assess reliability of the technique before proceeding. Intra- and inter-observer reliability was assessed with

intraclass correlation coefficients (ICC) using IBM SPSS Statistics 26 Software (IBM Corp.). Triplicate measurements by a single observer were performed for the remainder of the patient MRIs, and the median was used for evaluation. The first [10] MRIs with a median of <5cm^3 were used to assess the reliability of small tumour volumes and discern the lower limit of the segmentation technique. Segmented CE volumes were analyzed for differences between IDH mutation and MGMT methylation status for pre-operative volumes to assess if molecular profile influences contrast-enhanced tumour volume.

2.3.3 Volume of FLAIR hyperintense tumour tissue

Volume of T2 FLAIR hyperintense tissue was segmented and quantified using the same protocol described in section 2.3.2 and 2.3.3. T2 FLAIR images were acquired post-contrast injection, therefore the final volume included enhancing tumour tissue, non-enhancing tumour tissue and vasogenic edema seen as T2w hyperintensity. This was named the gross tumour (GT) ROI. An example of T2 FLAIR segmentation using the same MRI (WWS38A) as section 2.3.3 can be seen in Figure 10. Tumours with no contrast-enhancing component were only assessed for T2 FLAIR hyperintensity. MRIs exhibiting T2/FLAIR mismatch were first segmented on T2w images to create an ROI mask for the FLAIR sequence in order to include relatively low intensity solid tissue by correlating the sequences.

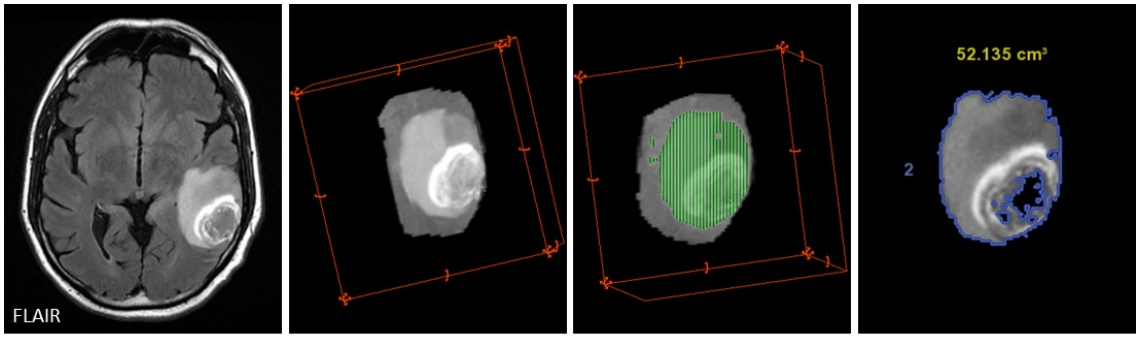

Figure 10. Segmentation of the GT on T2/FLAIR imaging.
Segmentation of the T2 hyperintense component of a GBM on T2/FLAIR imaging (WWS38A).

Triplicate measurements were again taken for WWS01A-06A by two observers for reliability assessment using ICCs. Triplicate measurements by a single observer were performed for the remainder of the patient MRIs and the median was used for evaluation. Segmented GT volumes were also analyzed for differences between IDH mutation and MGMT methylation status on pre-operative volumes to assess if molecular profile influences gross tumour volume. For all subsequent statistical tests, the results were considered statistically significant at significance level $\alpha < 0.05$. All statistical computations were performed with the statistical software package SPSS 26.0, Chicago, IL.

2.3.4 ROI cloning and ADC map analysis

Based on previous cut-off values for ADC thresholding suggested within the literature, the volumes of restricted tissue were measured on a $\mu m^2/s$ ADC map, at <4.0 (inclusive of all tissue), <1.5, <1.2, <1.0, <0.8, <0.6 and <0.5 cut-offs (Darbar et al., 2018; Orlandi et al., 2016; Lee et al., 2012; Kono et al., 2001). The threshold <1.2 and <1.0 were of particular importance for assessing differences in PsP and recurrence. As many studies

cite GBMs to have a mean ADC within the range of 0.363-0.820, the <1.0, <0.8, <0.6 and <0.5 thresholds were used to determine what volume of tumour tissue is this highly restricted (Darbar et al., 2018; Kono et al., 2001).

Once the two ROIs were created from the T2 FLAIR and T1w images, the CE ROI and the GT ROI were then cloned onto the ADC map ($\mu m^2/s$) by selecting *Clone to all series of exam*. The area outside the ROIs was the removed using *Cut all Outside* (Fig. 7d). The ADC maps were pre-processed for EPI correction and then a functional analysis summary table was used to display average, minimum and maximum ADC values as well as the volume (cm^3) within the two ROIs. The volume as well as the average ADC for the corresponding volume were recorded for both the GT and CE ROI at each of the chosen thresholds (Fig. 11). Thresholding could be applied bi-directionally, for example, highly restricted tissue could be excluded by applying a >0.8 low cut-off; however, for the purpose of this study, thresholds were only applied as high cut-offs.

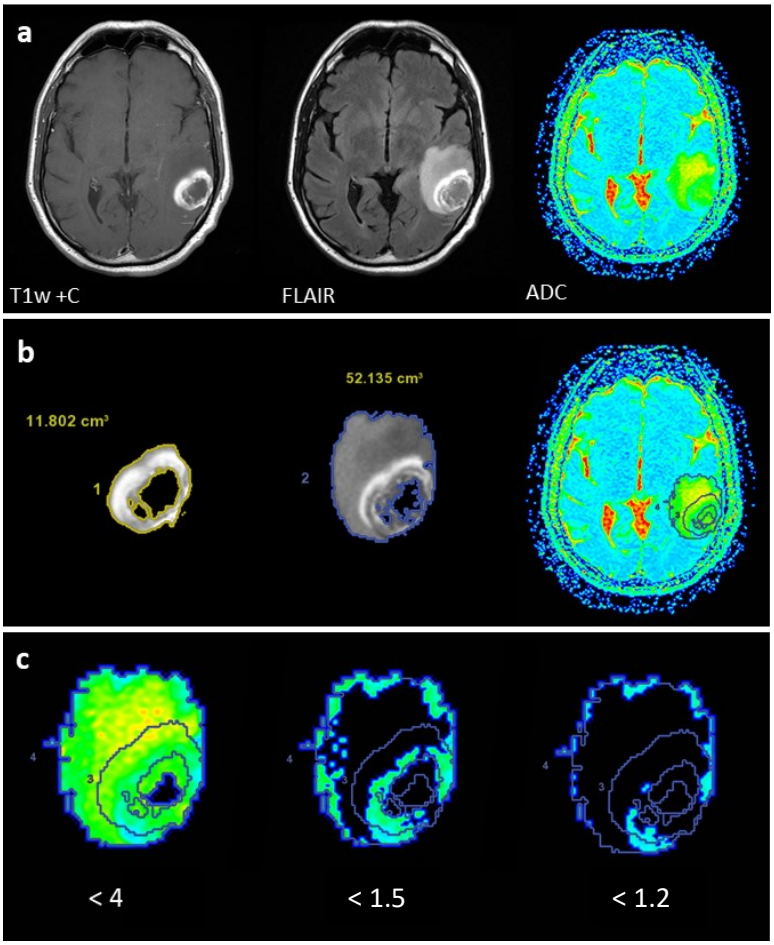

Figure 11. ROI cloning for ADC map analysis.
a) T1w contrast enhance, T2/FLAIR and ADC map of WWS38A MRI. b) Cloning ROIs of enhancing and non-enhancing tissue to ADC map. c) Thresholding of ADC map within ROIs ($\mu m^2/s$).

2.4 Correlation with EV RNA

The total Vn96-captured EV RNA yield per ml of plasma was available for 25 MRI time points of 10 patients. One RNA measure was excluded from analysis due to a duplication in MRI time points. An exploratory correlation analysis was performed on the naïve (normalized, untransformed) and log transformed RNA data to evaluate the relationship between RNA concentrations and corresponding tumour volumes for each MRI parameter. The MRI parameters assessed were: CE volume, GT volume, volumes with ADC <4, <1.5, <1.2 and <1 $\mu m^2/s$ for both CE and GT ROIs.

The naïve RNA data was normalized to ml of plasma (measured in ng) and was not normally distributed; therefore, a Spearman correlation matrix was used. Logarithmic transformation of the normalized RNA data was normally distributed; therefore, a Pearson correlation matrix was used. Both correlation matrices were performed in SPSS using two-tailed significance. Bonferroni correction for 10 variables was applied in both correlation studies, with results being statistically significant at the $p<0.005$ level.

CHAPTER 3 RESULTS

3.1 Patient Characteristics

A total of 40 patients were enrolled for MRI examination and of these, 6 patients were excluded for further analysis due to a history of previous tumour and resection (WWS19), non-standard imaging protocol (WWS17) or a final diagnosis other than glioma (WWS11, 24, 34 and 35). The 34 patients included in the analysis had a mean age of 57.4 ± 14.1 years (range 31—78) and consisted of 20 males and 14 females. 31 patients to date have undergone surgical resection and 26 have started chemoradiotherapy. The average length of follow up was 10.3 months at the time of data analysis (Fig. 12). A total of 129 MRI exams were included in analysis.

Patients with GBM had a mean age of 61.7 ± 11.4 years (range 37—78) and consisted of 16 males and 10 females. Patients with lower grade gliomas had a mean age of 43.3 ± 13.2 years (range 31—66) and consisted of 4 males and 4 females. Of the non-GBM tumours, 2 patients were diagnosed with an oligodendroglioma, 1p/19q co-deletion, 5 patients were diagnosed with a grade 2 astrocytoma, IDH-mutant and 1 patient with a grade 3 glioma *NOS*. The mean time to surgery from pre-operative (A) MRI was 5.32 days for GBM patients and 32.5 days for non-GBM patients.

In the 34 patients enrolled in this study, MGMT promotor methylation was present in 21 patients (62%) and 9 patients had an IDH mutation. Further patient characteristics can be found in appendices, Table 22.

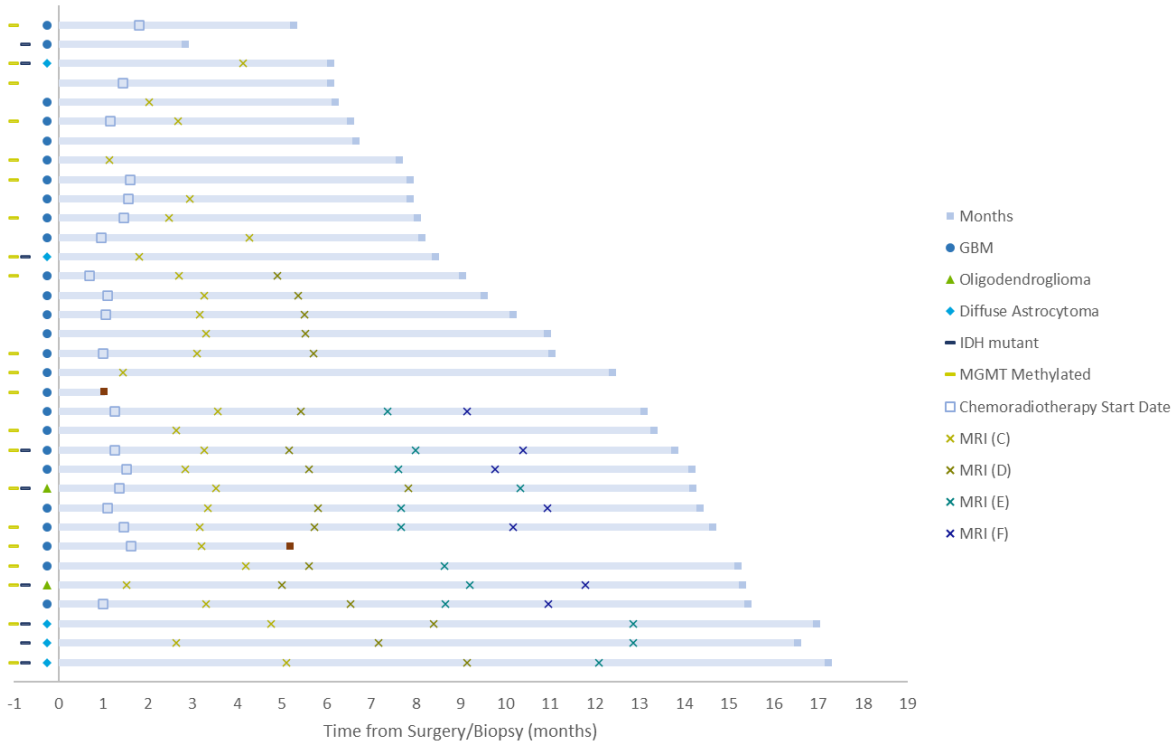

Figure 12. Patient follow-up timeline.
Time (months) since surgery/biopsy. Pathology and IDH mutant and MGMT methylation status are denoted on the left for each patient. Sequential MRIs are marked by an x on the patient's timeline and are colour coded according to group (C, D, E and F). Bars with a red mark denote patients whom are deceased.

3.2 Image Post-Processing Reliability

The reliability assessment of WWS01-WWS06 performed by two raters using triplicate measurements showed excellent intra-rater and inter-rater reliability for the contrast-enhanced (T1w CE) and FLAIR hyperintense volume measurements (Figure 13). The 6 patients selected for the reliability assessment included 5 GBMs and 1 Oligodendroglioma (WWS04) and illustrated a broad range of tumour appearances. Segmented CE and FLAIR volumes used in the reliability assessment included tumours with multifocal lesions, high motion artifacts, central necrotic cores and lesions with

close proximity to other brain structures. The ICCs of tumour volumes are shown in Table 2.

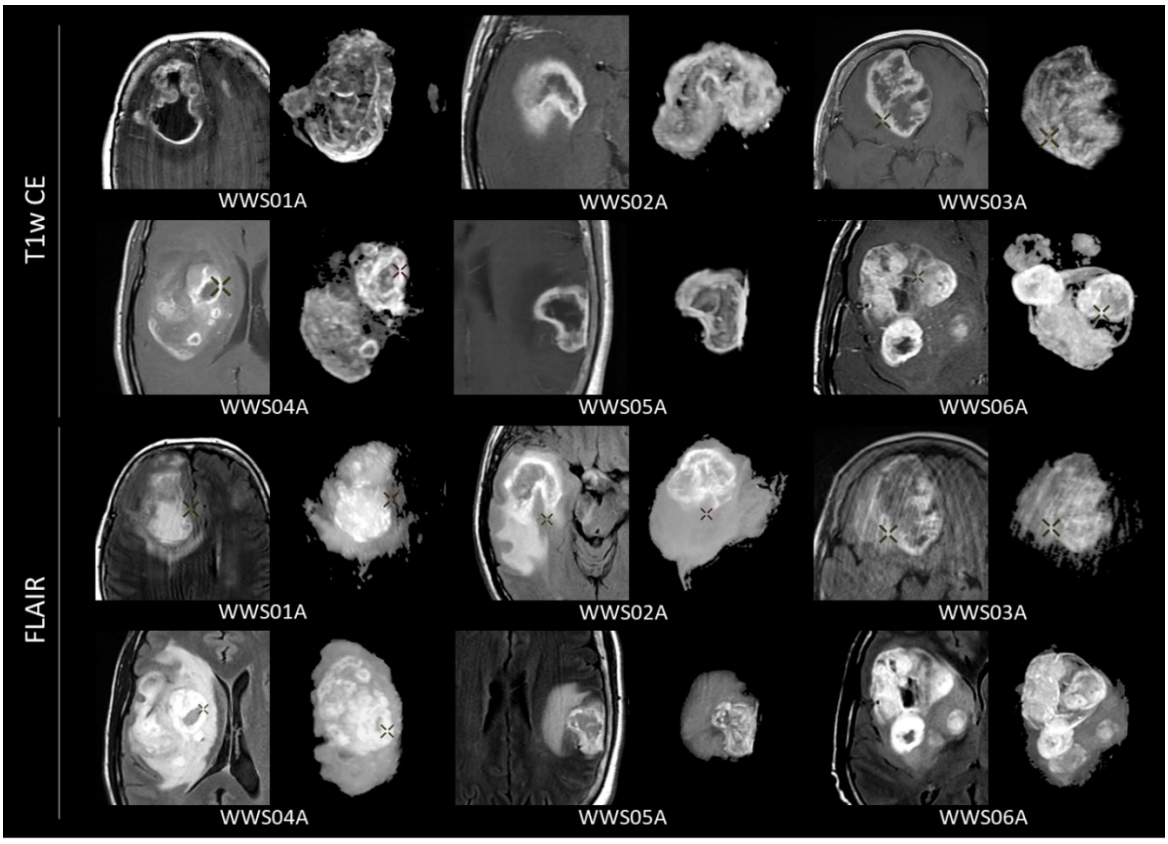

Figure 13. Segmented CE and GT volumes included in reliability study.
Segmented CE tumour tissue on T1w gadolinium enhanced and GT tissue on T2 FLAIR with axial reference images for 6 patients' pre-operative MRIs (WWS01A-06A).

Table 2. ICCs for segmentation reliability.
ICCs with 95% confidence intervals for trained and novice rater on T1w CE and FLAIR MRI contrasts.

Contrast	Rater	ICC	Sig.
T1w CE	Intra-observer: *Trained*	.983 (0.930-0.997)	0.000
T1w CE	Intra-observer: *Novice*	.904 (0.662-0.985)	0.000
T1w CE	Inter-observer	.991 (0.938-0.999)	0.000
FLAIR	Intra-observer: *Trained*	.976 (0.903-0.996)	0.000
FLAIR	Intra-observer: *Novice*	.930 (0.743-0.989)	0.000
FLAIR	Inter-observer	.990 (0.927-0.999)	0.000

Intra-observer and inter-observer reliability was excellent for all parameters, suggesting the segmentation protocol was reliable for the analysis of further MRI examinations. The practiced rater consistently showed higher intra-observer reliability than the novice rater. The more practised rater consistently achieved coefficients of variation < 10%. Assessment of CE volumes with a median <5cm^3 showed an ICC of 0.795 (0.526-0.939), suggesting good reliability in measuring small lesions, however lower reliability than tumour volumes >5cm^3.

3.3 Segmented Tumour Volumes

A total of 111 CE and 111 GT volumes were segmented from the available serial MRIs. A variety of segmented CE and GT volumes can be seen in Figure. 14. WWS27 exemplifies a relatively straightforward CE and GT segmentation with central necrotic core that could not be measured according to RANO criteria. Other examples were chosen in order to visualize segmentations of tumours with irregular CE rims (WWS33A) or multifocal, minimally enhancing or small (1.5cm^3) CE lesions (WWS07A, WWS13A and WWS39A respectively). Tumours with blurred boundaries (WWS26A), multifocal (WWS21A) and extensive (WWS11A) T2/FLAIR lesions that are typically considered non-measurable as well as segmented volumes of challenging cases such as tumours with close proximity to adjacent fat from the scalp (WWS38C) or an orbit (WWS40A) and a resection cavity (WWS28C) are also depicted in Fig. 14.

For contrast-enhancing (CE) tumour tissue, the mean preoperative tumour volume was 24.56 ± 16.51 cm^3 for GBMs. Figure 15 depicts the CE volumes for patients with a

minimum of 3 serial MRI time points. Table 3 shows the median CE tumour volumes for all MRIs. The average standard deviation for all CE measurements was 1.23 cm^3.

For GT volumes, the mean preoperative volume was 93.8 ± 42.3 cm^3 for GBMs and 50.77 ± 44.9 cm^3 for non-GBM gliomas. Table 4 shows the median GT volumes for all patients' MRIs. The average standard deviation for all GT measurements was 4.14 cm^3.

Analysis of all patients that had maximal safe resection with a B scan available showed the average percent of CE tissue resected was 66 ± 33 % (n=24). 11 patients had resections of over 80% and 5 of these were >90%.

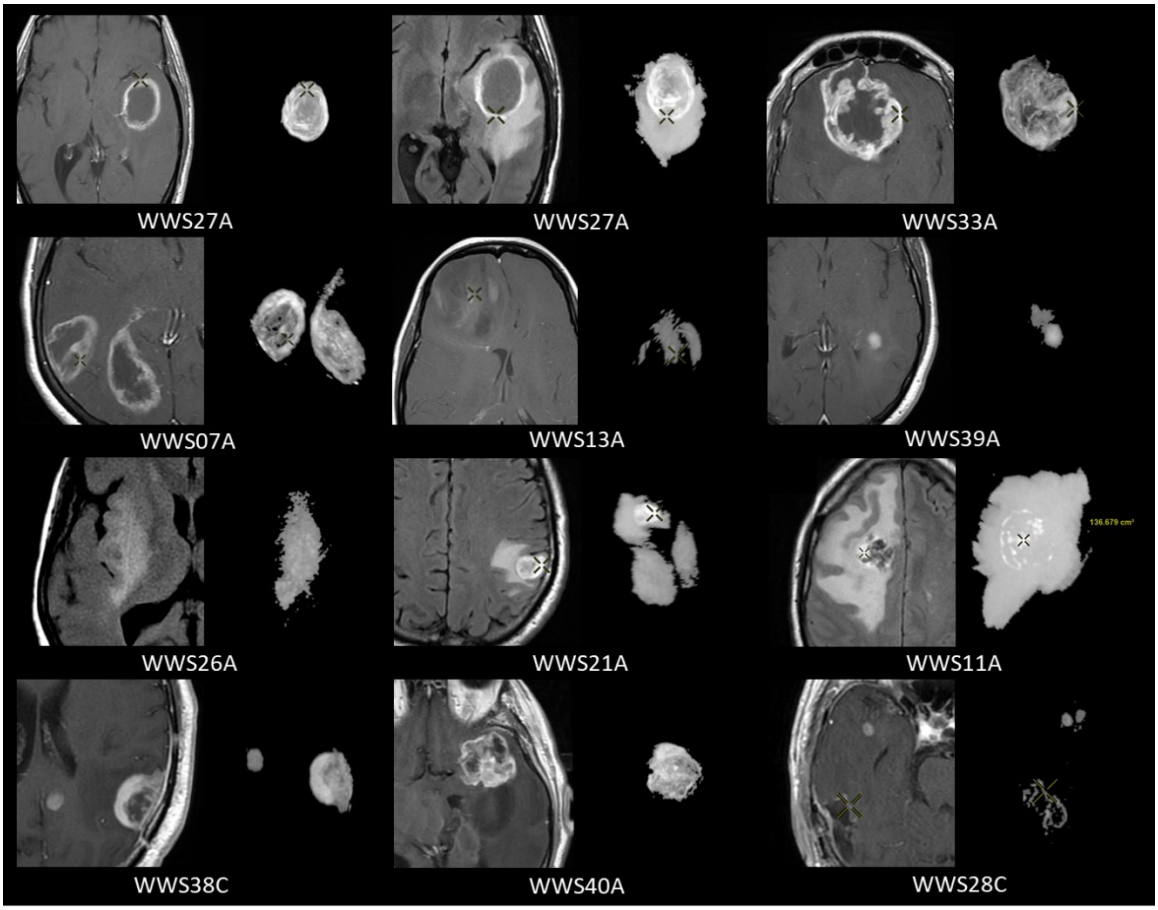

Figure 14. Segmented CE and GT volumes of example subjects.
Segmented tumours with axial reference image for 12 patients on T1w CE or T2/FLAIR MRI contrasts.

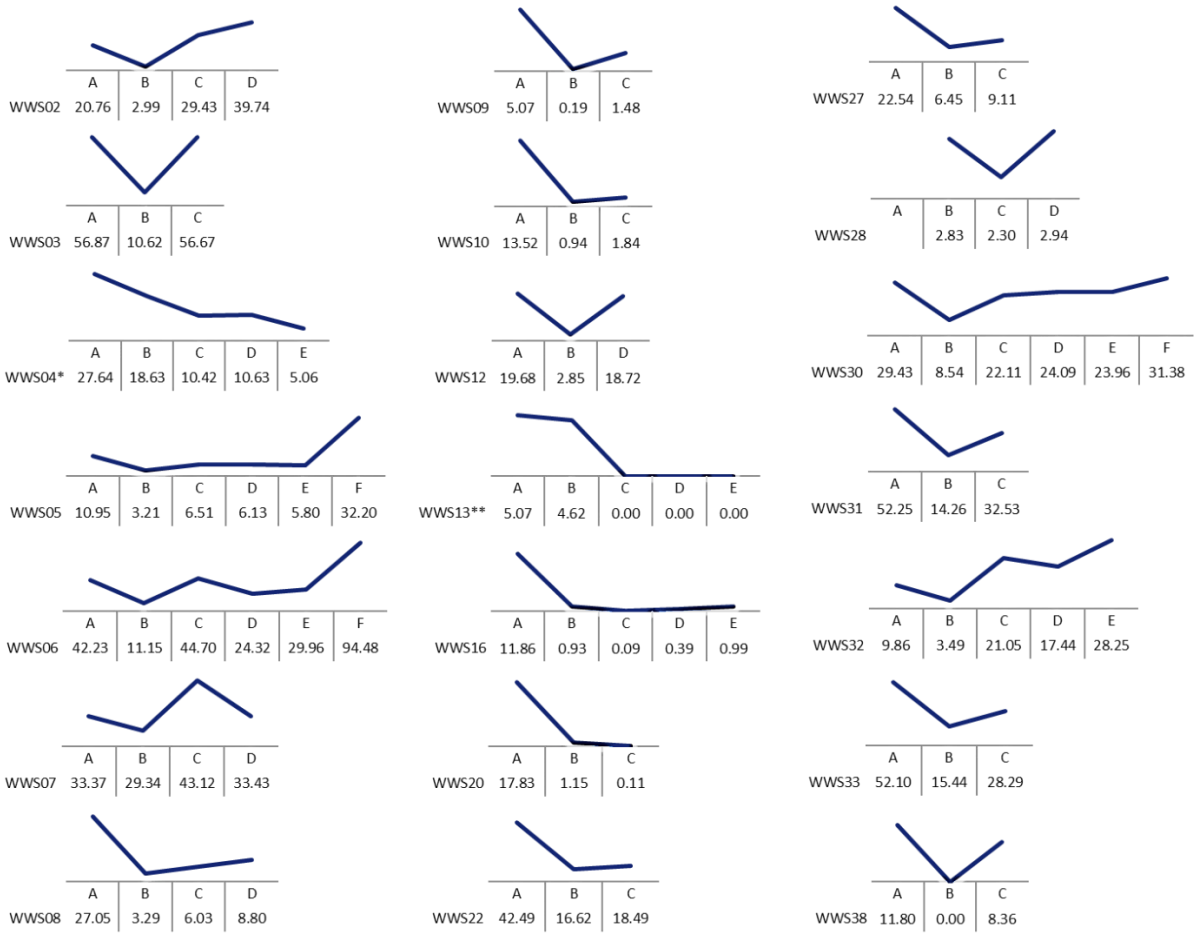

Figure 15. CE Tumour Volumes for serial MRIs. Data tables include categorical time points and median volumes in cm^3. Patients with fewer than 3 MRIs were excluded from figure.

Average pre-operative GT volumes were significantly larger (p=0.02) for IDH wild-type gliomas (99.7 ± 45.8 cm^3) than IDH-mutant gliomas (56.3 ± 43.8 cm^3) (Fig. 16). Pre-operative CE volumes were also significantly different for IDH-mutant and IDH wild-type gliomas (p=0.007); however, there was no significant difference when excluding patients with no contrast enhancing lesion due to T2/FLAIR mismatch. No significant differences were found between MGMT methylated and non-methylated gliomas for both CE and GT volumes.

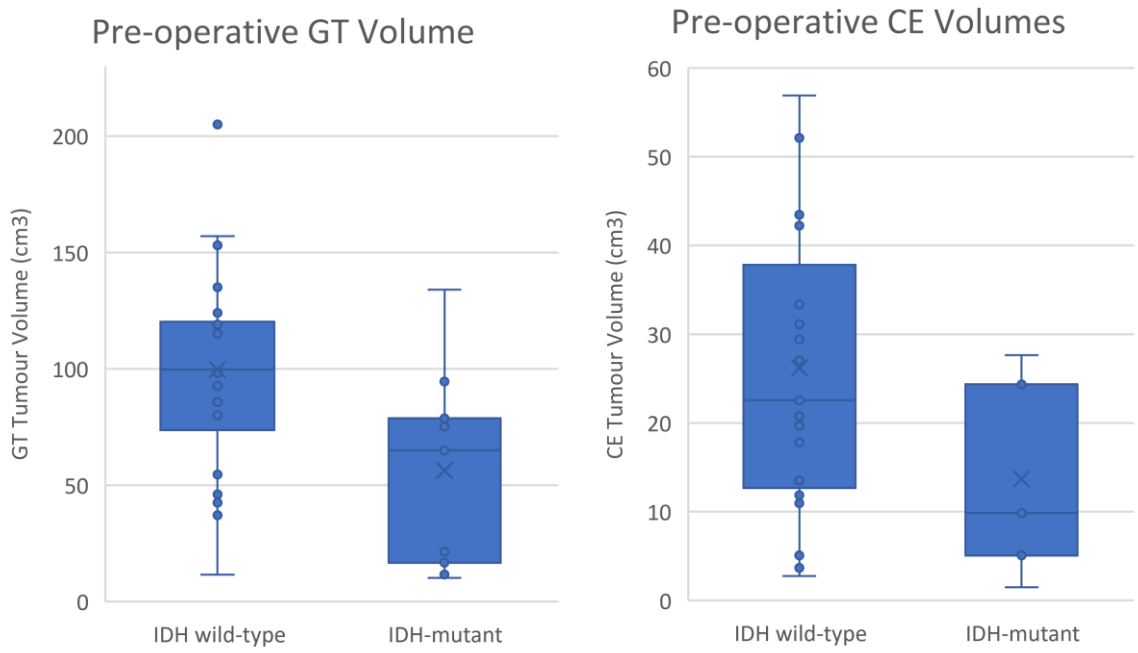

Figure 16. Pre-operative GT and CE volumes for IDH mutant and IDH wild-type gliomas.
Pre-operative CE volumes box blot excluding gliomas with no CE lesion (p=0.115).

Table 3. Median CE Tumour Volumes.

Patient	A	B	C	D	E	F
WWS01	31.84 ± 0.32	4.04 ± 0.37				
WWS02	20.76 ± 0.98	2.99 ± 0.86	29.43 ± 2.04	39.74 ± 1.71		
WWS03	56.87 ± 6.06	10.62 ± 0.20	56.67 ± 1.04			
WWS04*	27.64 ± 0.63	18.63 ± 2.30	10.42 ± 3.57	10.63 ± 0.42	5.06 ± 0.57	
WWS05	10.95 ± 0.67	3.21 ± 0.78	6.51 ± 1.37	6.13 ± 2.06	5.80 ± 0.28	32.20 ± 2.21
WWS06	42.23 ± 1.95	11.15 ± 0.96	44.70 ± 4.50	24.32 ± 2.77	29.96 ± 3.46	94.48 ± 2.18
WWS07	33.37 ± 0.68	29.34 ± 0.57	43.12 ± 0.31	33.43 ± 0.83		
WWS08	27.05 ± 0.21	3.29 ± 0.68	6.03 ± 1.32	8.80 ± 1.01		
WWS09	5.07 ± 0.06	0.19 ± 0.34	1.48 ± 0.41			
WWS10	13.52 ± 0.12	0.94 ± 0.26	1.84 ± 0.13			
WWS12	19.68 ± 1.39	2.85 ± 0.49		18.72 ± 0.42		
WWS13**	5.07 ± 1.29	4.62 ± 0.43	0.00 ± 0.00	0.00 ± 0.00	0.00 ± 0.00	
WWS14**	0.00 ± 0.00	0.00 ± 0.00	0.38 ± 0.17	0.00 ± 0.00		
WWS15**	0.00 ± 0.00		0.00 ± 0.00	0.52 ± 0.07	0.72 ± 0.08	
WWS16	11.86 ± 1.49	0.93 ± 0.08	0.09 ± 0.00	0.39 ± 0.07	0.99 ± 0.04	
WWS18**	0.00 ± 0.00	0.00 ± 0.00	0.00 ± 0.00			
WWS20	17.83 ± 1.10	1.15 ± 0.87	0.11 ± 0.01			
WWS21	3.69 ± 0.13		2.79 ± 0.43			
WWS22	42.49 ± 3.79	16.62 ± 0.65	18.49 ± 2.06			
WWS23	31.13 ± 1.75	41.96 ± 4.14				
WWS25	43.46 ± 4.66	7.33 ± 0.28				
WWS26	2.75 ± 1.04					
WWS27	22.54 ± 1.89	6.45 ± 2.00	9.11 ± 0.19			
WWS28		2.83 ± 0.18	2.30 ± 0.63	2.94 ± 0.23		
WWS29*	24.34 ± 0.64					
WWS30	29.43 ± 1.20	8.54 ± 1.69	22.11 ± 0.94	24.09 ± 0.40	23.96 ± 1.33	31.38 ± 1.04
WWS31	52.25 ± 4.80	14.26 ± 0.97	32.53 ± 2.25			
WWS32	9.86 ± 1.18	3.49 ± 1.89	21.05 ± 4.03	17.44 ± 2.23	29.07 ± 3.84	
WWS33	52.10 ± 1.86	15.44 ± 1.39	28.29 ± 0.66			
WWS36***	0.00 ± 0.00	0.00 ± 0.00				
WWS37**	0.00 ± 0.00	0.00 ± 0.00				
WWS38	11.80 ± 0.98	0.00 ± 0.00	8.36 ± 0.30			
WWS39	1.50 ± 0.09					
WWS40	19.95 ± 0.65	13.88 ± 0.67				

* Oligodendroglioma

** Astrocytoma Grade 2

*** *NOS*

Table 4. Median GT Tumour Volumes.

Patient	A	B	C	D	E	F
WWS01	107.39 ± 2.29	59.75 ± 1.08				
WWS02	158.09 ± 3.61	147.73 ± 1.88	185.72 ± 0.13	202.28 ± 4.69		
WWS03	117.76 ± 6.01	87.52 ± 2.19	65.89 ± 1.54			
WWS04*	133 ± 4.28	93.91 ± 1.44	36.11 ± 5.38	108.14 ± 0.85	99.17 ± 6.71	
WWS05	33.82 ± 1.54	34.18 ± 0.03	115.35 ± 3.18	63.58 ± 1.46	69.75 ± 6.13	100.16 ± 6.84
WWS06	137.87 ± 10.0	98.00 ± 1.10	179.81 ± 9.98	91.15 ± 5.92	125.66 ± 7.24	239.34 ± 23.6
WWS07	118.4 ± 0.53	65.61 ± 5.07	107 ± 6.18	46.29 ± 4.47		
WWS08	97.53 ± 2.46	55.21 ± 0.63	20.25 ± 3.23	35.69 ± 3.72		
WWS09	90.94 ± 1.57	85.11 ± 0.81	3.40 ± 0.63			
WWS10	40.78 ± 2.12	10.08 ± 0.64	1.90 ± 0.96			
WWS12	120.96 ± 4.81	81.79 ± 1.13		117.99 ± 2.84		
WWS13**	90.88 ± 4.52	27.11 ± 2.92	21.77 ± 2.00	23.38 ± 1.66	23.105 ± 1.52	
WWS14**	12.7 ± 1.66	13.29 ± 0.21	8.045 ± 1.20	3.12 ± 0.32		
WWS15**	11.51 ± 1.17		23.35 ± 1.87	24.78 ± 1.08	6.375 ± 0.72	
WWS16	69.6 ± 6.61	55.78 ± 4.10	14.68 ± 1.70	10.93 ± 1.22	16.33 ± 0.62	
WWS18**	16.27 ± 0.40	15.59 ± 0.01	5.23 ± 0.62			
WWS20	97.08 ± 2.39	77.09 ± 5.44	16.85 ± 1.34			
WWS21	37.33 ± 4.79		30.24 ± 2.71			
WWS22	115.71 ± 1.77	80.90 ± 3.51	53.11 ± 0.96			
WWS23	74.6 ± 6.54	123.7 ± 17.44				
WWS25	75.41 ± 6.38	48.98 ± 1.47	51.15 ± 1.99			
WWS26	13.05 ± 5.35					
WWS27	85.74 ± 4.04	85.87 ± 1.16				
WWS28		88.53 ± 13.57	64.88 ± 13.77	107.56 ± 2.10		
WWS29*	77.55 ± 0.75					
WWS30	101.8 ± 7.29	90.80 ± 3.18	97.96 ± 1.86	158.14 ± 5.30	96.79 ± 5.83	183.33 ± 2.45
WWS31	108 ± 5.30	56.53 ± 1.72	31.3 ± 0.86			
WWS32	72.53 ± 6.70	43.52 ± 3.00	28.66 ± 2.12	57.05 ± 6.17	185.93 ± 16.1	
WWS33	202 ± 7.82	133.99 ± 7.05	76.55 ± 2.81			
WWS36***	42.12 ± 2.79	39.53 ± 2.79				
WWS37**	22.12 ± 1.10	16.56 ± 0.41				
WWS38	52.13 ± 1.32	40 ± 0.93	58.59 ± 3.72			
WWS39	74.54 ± 2.14					
WWS40	141.77 ± 3.54	144.03 ± 6.44				

* Oligodendroglioma

** Astrocytoma Grade 2

*** *NOS*

3.4 ADC map analysis

Average ADC for all pre-operative CE tumour volumes was 1.24 ± 0.18 $\mu m^2/s$ and 1.37 ± 0.16 $\mu m^2/s$ for GT tumour volumes. WWS26 (GBM, MGMT non-methylated and IDH wild-type) had the lowest ADC average for the CE component (1.06 $\mu m^2/s$), whereas WWS32 (GBM, MGMT methylated, IDH-mutant) had the highest ADC average for the CE component (1.78 $\mu m^2/s$).

Significant ADC differences related to IDH mutational status could not be observed in CE volumes (averaged 1.23 $\mu m^2/s$ in IDH wild-type gliomas compared with 1.31 $\mu m^2/s$ in IDH mutant gliomas) or GT volumes (averaged 1.37 $\mu m^2/s$ IDH wild-type and 1.39 $\mu m^2/s$ IDH mutant). Similarly, no significant differences were found between mean ADC values for MGMT methylation status for both CE and GT ROIs.

GBM patients were found to have a mean ADC of 1.24 ± 0.18 $\mu m^2/s$ for the preoperative CE component of the tumour. The mean preoperative CE volume with ADC values <0.8 $\mu m^2/s$ was 1.5 ± 1.6 cm^3 for GBM patients, comprising only a very small portion of the total CE volume.

Three cases of resected GBMs with follow-up clinical diagnoses are depicted in Figures 17, 18 and 19. Two cases were labelled as having PsP (Fig.17 and 18) and one case of recurrence (Fig.19). The volumetric ADC histograms for both CE and GT ROIs are shown for each case.

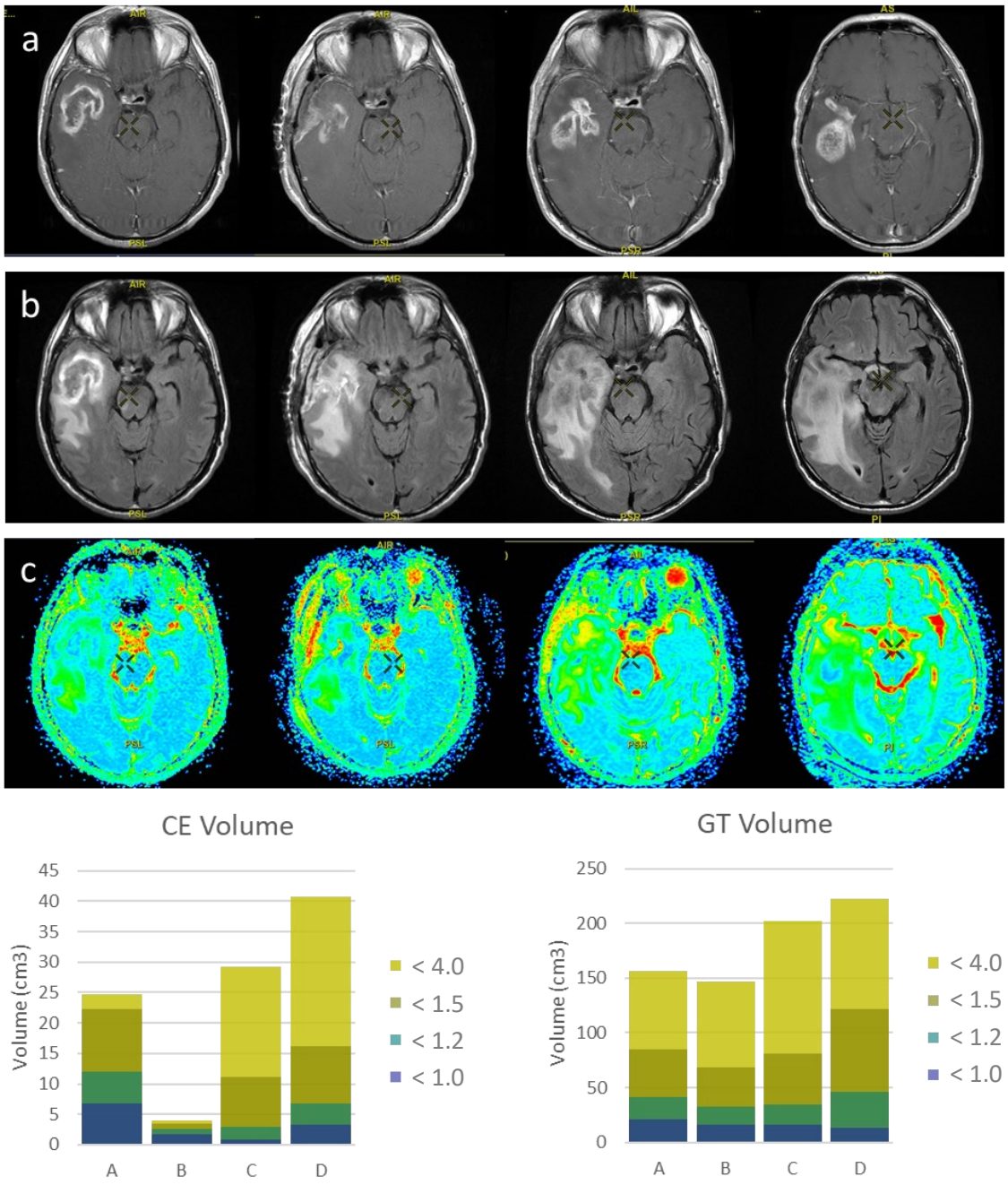

Figure 17. ADC analysis of a 63-year-old male patient with a clinical diagnosis of Pseudoprogression of a GBM

CE T1w (a), FLAIR (b) and ADC parametric maps (c) of serial MRIs of WWS02 for time points A, B, C and D and resulting quantitative histogram. Volumes are plotted in cm^3 and colour coded according to ADC ($\mu m^2/s$) threshold (<4, <1.5, <1.2 and <1). Surgical resection removed 86% of the pre-operative CE volume. PsP was diagnosed at time point C and D.

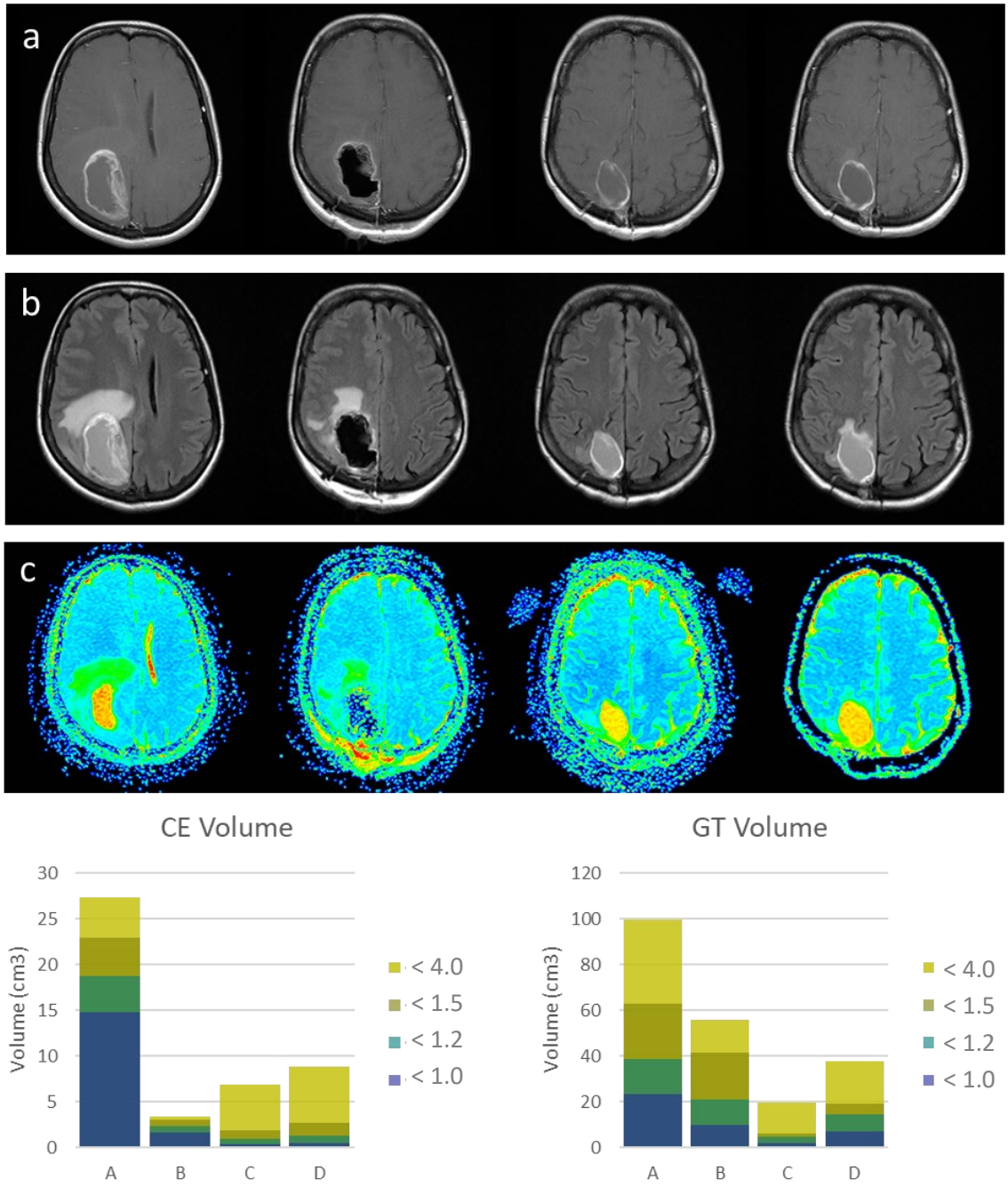

Figure 18. ADC analysis of a 38-year-old female patient with a clinical diagnosis of Pseudoprogression of a GBM.

CE T1w (a), FLAIR (b) and ADC parametric maps (c) of serial MRIs of WWS08 for time points A, B, C and D and resulting quantitative histogram. Volumes are plotted in cm^3 and colour coded according to ADC ($\mu m^2/s$) threshold (<4, <1.5, <1.2 and <1). Surgical resection removed 88% of the pre-operative CE volume. PsP was diagnosed at time point C and D.

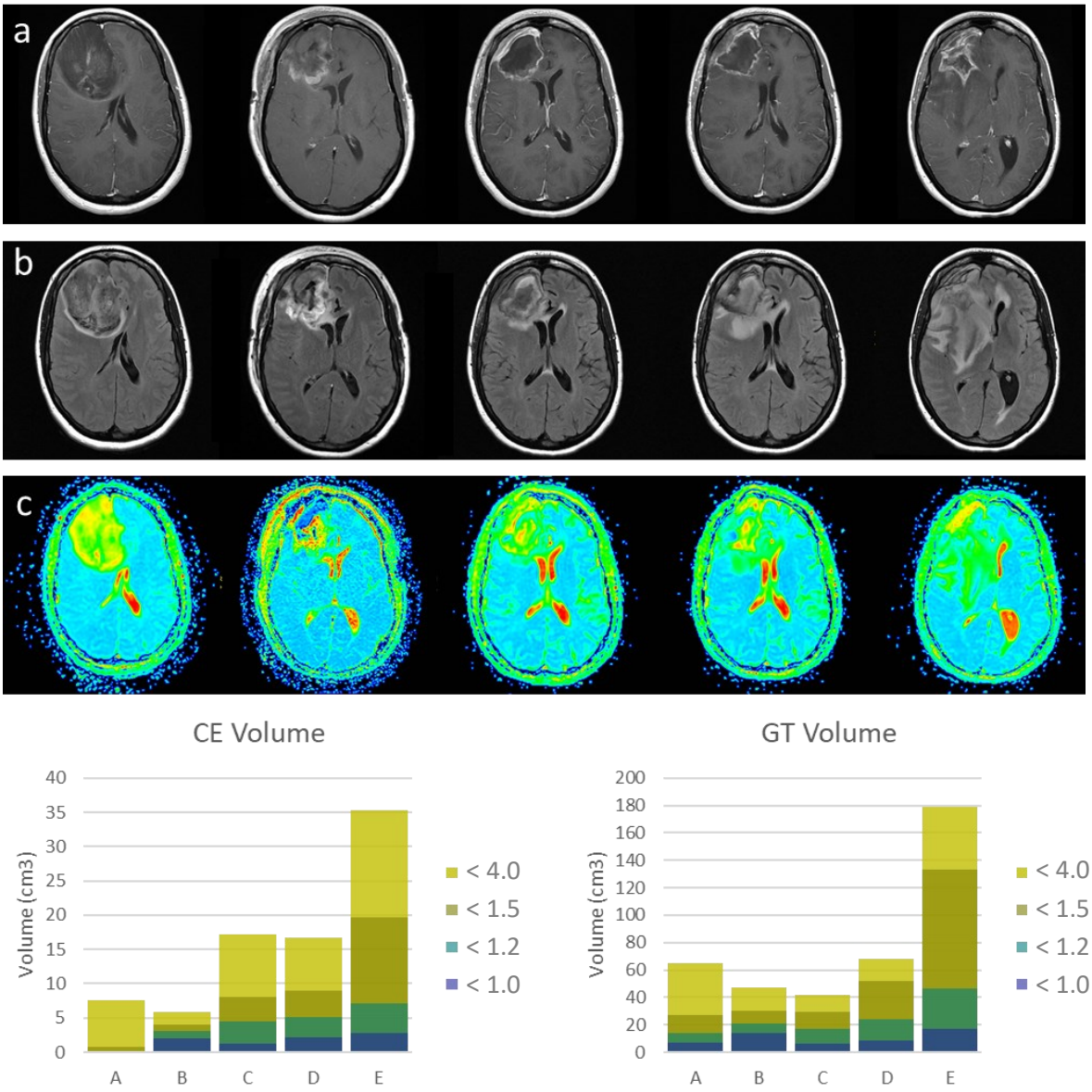

Figure 19. ADC analysis of a 38-year-old female patient with a clinical diagnosis of recurrence of a GBM.

CE T1w (a), FLAIR (b) and ADC parametric maps (c) of serial MRIs of WWS32 for time points A, B, C, D and E, with corresponding quantitative histograms. Volumes are plotted in cm^3 and colour coded according to ADC ($\mu m^2/s$) threshold (<4, <1.5, <1.2 and <1). Surgical resection removed 65% of the pre-operative CE volume. Recurrence was diagnosed at time point E.

3.5 Correlation with EV RNA

The 10 patients with RNA measures (ng of RNA/ mL of plasma from liquid biopsy) included 9 GBMs and 1 oligodendroglioma. The correlation matrices were run with 8 variables: [RNA], CE volume, FLAIR volume, and ADC volumes within masks defined by the two ROIs (CE and GT) for 4 thresholds (<4, <1.5, <1.2 and <1 $\mu m^2/s$). The thresholds <0.8, <0.6 and <0.5 were excluded due to patients having little or no tumour volume under these levels of ADC thresholding. The Spearman correlation analysis using the naïve RNA data did not yield any significant results.

Using the transformed data, an initial correlation matrix was run using all 10 patients with a total of 24 measures at different MRI time points. Pearson correlation of GT volume of tumour tissue with an ADC <1 showed a significant positive correlation with RNA concentration (r=0.608, p=0.002).

The patient with the oligodendroglioma was then excluded from the correlation matrix to assess the relationship between RNA concentration and GBM features exclusively. The remaining 9 patients had a total of 22 RNA measures at various MRI time points. Of the patients included in the RNA correlation study, 1 patient (WWS32) was a GBM IDH-mutant, MGMT methylated, two patients (WWS30 and WWS08) were a GBM IDH wild-type with MGMT methylation and the remaining 6 patients were GBM IDH wild-type, MGMT non-methylated.

Pearson correlation of CE volume of tumour tissue with an ADC <1 $\mu m^2/s$ showed a significant positive correlation with RNA concentration (r=0.581). In addition, GT tumour

volumes with ADC <1.2 and <1 showed significant positive correlations with RNA concentration (0.583 and 0.684) (Figures 20 and 21).

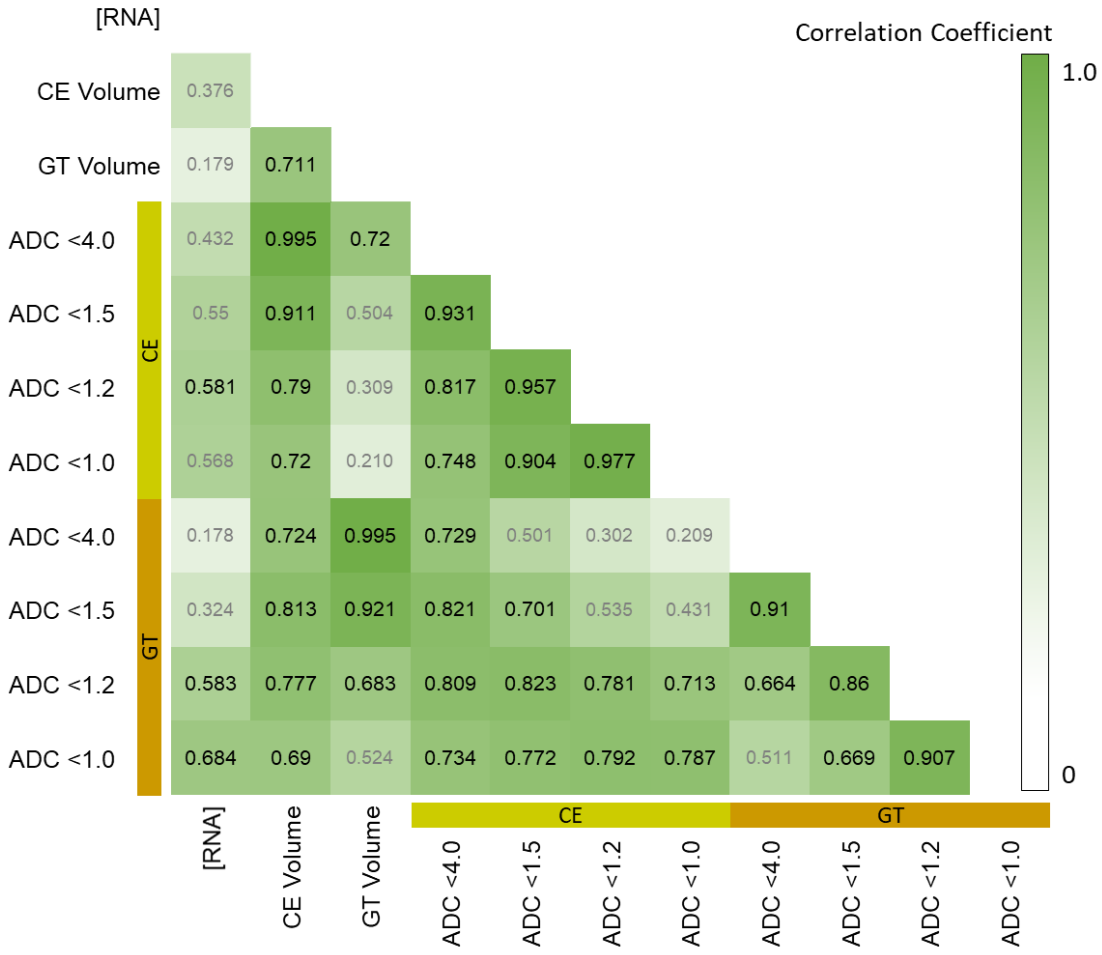

Figure 20. Correlations between tumour volumes and RNA concentration.
A correlation heatmap (Pearson r) of Tumour Volumes and RNA samples. [RNA] is log(RNA) in ng normalized to ml of plasma. Significant correlations ($p<0.005$) are highlighted in black.

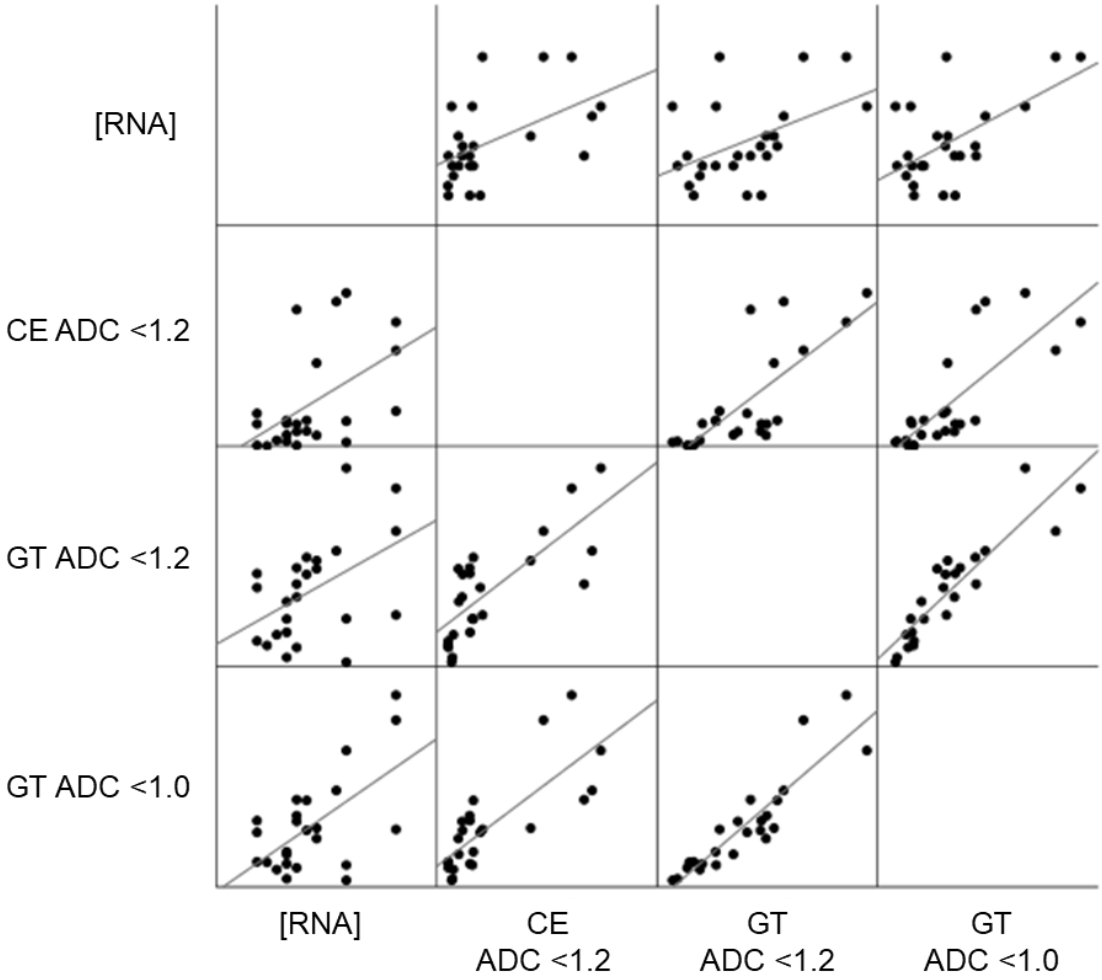

Figure 21. Scatterplot matrix of significant correlations between ADC tumour volumes and RNA concentration.

[RNA] is log(RNA) in ng normalized to ml of plasma. All correlations were significant at the $p<0.005$ level.

CHAPTER 4 DISCUSSION

Gliomas can be difficult to quantify for clinical study. Standard methods of assessment (e.g. RANO criteria) and subjective evaluation of images leave uncertainty with regard to factors that influence tumour burden, such as overall size, amount of non-enhancing tumour tissue and cellularity. Having reliable measures of tumour volume is crucial for comparing MRI features to novel biomarkers, such as EV counts and RNA concentrations from liquid biopsies. Therefore, my goal was to develop a reliable method to assess tumour features quantitatively on several MRI contrasts.

4.1 Segmentation on MRI

This study used a manual segmentation approach, with a hybrid of boundary and threshold-based segmentation that assesses 5 MRI contrasts: T1, T1c, T2, T2 FLAIR, ADC/DWI, and it can also be applied to perfusion imaging for rCBV/rCBF ROIs. This segmentation technique has high inter- and intra-observer reliability. However, it should be acknowledged that inter-rater reliability may have been augmented as initial training on assessing brain tumour features on MRI was given by the second rater (experienced neuroradiologist, Schmidt. M). A practised rater can detect changes in the volume of gadolinium-enhancing tissue and FLAIR hyperintense tissue ≥ 10%. Importantly, the 6 patients included in the reliability study represented a spectrum of tumour appearances that displayed a wide variety of factors that could influence measurement error, such as multifocal lesions, large necrotic cores, blurred boundaries and severe motion artifacts

(Fig. 13). Despite this variability among tumours, reliability for both CE and GT volumes was excellent, ranging from 0.93-0.991 across raters and MRI contrasts (Table 2).

The use of complex algorithms in tumour segmentation techniques is a key reason to why segmentation techniques are often not adopted into practice (Menze et al., 2015; Wadhwa et al., 2019).

The benefit of the present technique is that it is simple and does not rely on the implementation of new, complex algorithms. It only requires an understanding of the neuroimaging features and behaviour of gliomas and familiarity with standard clinical image analysis software. Thus, it can be taught to clinicians and radiologists, the intended target audience.

All MRI examinations in this study were performed as part of routine clinical care, and the image post-processing utilized tools embedded within readily available clinical software. All examinations in this study were performed with the same 1.5T MRI scanner using the same imaging parameters. This can be a barrier in longitudinal studies if different scanners are used resulting in varying imaging parameters (Reimer et al., 2017). Therefore, replication of the current study and technique should be performed with other MRI scanners (such as a 3T scanner) to ensure that the results of this study can be generalized.

This segmentation technique has the capacity to evaluate all serial MRIs throughout the disease timeline, including post-operative MRI scans with surgical resection cavities (Fig. 14). This allows the volume of tumour tissue resected during surgery to be quantified.

This is vital information as the percent of tumour tissue surgically resected is a known factor in influencing survival outcomes (Lacroix et al., 2001). Moreover, having the ability to quantify tumour tissue in serial MRIs allows for individual patients' CE and GT volumes to be tracked longitudinally and thus monitor their disease progression and treatment effects quantitatively (Fig. 15, Tables 3 amd 4).

This technique also has the ability to quantify non-enhancing T2 hyperintense tissue which includes peritumoral edema and non-enhancing solid tumour tissue. These non-enhancing components have key roles in tumour growth and invasion, as well as neurological symptoms (Dallabona et al., 2017; Schoenegger et al., 2009; Leao et al., 2020). It is now well known that neoplastic infiltration of cancer cells is present within peritumour edema, yet there is no standard for measuring T2 hyperintensity. Having a reliable technique for quantifying T2 hyperintensity is needed to assess the prognostic implications of non-enhancing tumour tissue.

Lastly, when quantifying non-enhancing tumour tissue, there was significant higher GT volumes in IDH wild-type (99.7 cm^3) than IDH-mutant (56.3 cm^3) gliomas (Fig. 18). This is consistent with the literature that IDH wild-type gliomas typically carry a worse prognosis and evidence suggesting that extensive peritumoural edema may contribute to shorter survival times (Lacroix et al., 2001). It is also known that peritumoral edema is a common feature of high-grade gliomas such as GBM IDH wild-type (Schoenegger et al., 2009; Wick et al., 2013; Reifenberger et al., 2017). Interestingly, CE tumour volume was not significantly different between IDH mutational status when gliomas with

T2/FLAIR mismatch sign were excluded (Fig. 16). This is likely a result of low statistical power as 5/9 IDH-mutant gliomas exhibited T2/FLAIR mismatch and no-enhancing component.

4.2 ADC map analysis

DWI allows the non-invasive assessment of tumour cellularity as cellular structures impede water movement, resulting in areas of high and low cellular density throughout the tumour tissue (Kwee et al., 2010). ADC is the most common measure of diffusion restriction, with areas of high cellular density exhibiting low ADC values, such as solid tumour tissue, and areas of low cellular density exhibiting higher ADC values (Lee et al., 2012). ADC measures have been studied extensively for brain tumour characterization and differentiation of PsP from recurrence (Kwee et al., 2010; Hygino et al., 2011; Van Dijken et al., 2017).

Although several studies have found the mean ADC of GBMs to be within 0.363-0.820 $\mu m^2/s$ (Kono et al., 2001; Darbar et al., 2018), in the present study GBM patients had a mean ADC of 1.245 ± 0.18 $\mu m^2/s$ for the CE tumour volume. This is likely due to the use of point ROIs to evaluate ADC values in prior studies, biasing toward areas of highly restricted tissue. My findings suggest that only a small portion of the CE tissue in glioma patients has ADC <0.8 $\mu m^2/s$, and that applying multiple thresholds to the ADC map for both CE and GT volumes provides a more comprehensive assessment for the purpose of evaluating changes in cellularity over time.

Consistency in ADC studies has also been reduced by examining heterogeneous patient groups with different tumour grades. Optimal cut-off values to distinguish between PsP and recurrence may vary, depending on the molecular profile of the tumour. Since GBM IDH wild-type and GBM IDH-mutant are now regarded as different tumours, the latter now being classified as Astrocytoma IDH-mutant grade 4, it is important to ensure these tumours are evaluated separately as this has likely influenced ADC cut-off values within the literature (Louis et al., 2021; Reimer et al., 2017). This heterogeneity of included patients can also make direct comparison between studies extremely difficult. Although IDH-mutant gliomas had higher mean ADC values in the present study (1.31 and 1.39 $\mu m^2/s$ for CE and GT volumes, respectively) than IDH-wildtype gliomas (1.23 and 1.37 $\mu m^2/s$ for CE and GT volumes), this difference was not statistically significant. This may be due to the limited number of patients with IDH-mutations (n=9).

Lastly, a limitation of many studies evaluating PsP vs progression is that both entities may exist simultaneously within the tumour tissue. Three cases were chosen to examine this phenomenon and how this may be reflected in ADC values (Figures 17-19).

In the case of WWS02, an IDH wild-type, MGMT non-methylated GBM (Fig. 17), time points C and D were clinically determined to be PsP. We can see a large increase in the enhancing component with lower cellularity (ADC > 1.2 $\mu m^2/s$), suggesting PsP at time point C and D, congruent with the diagnosis. However, when comparing time point D to C there was a large increase in volume of CE tissue with an ADC value < 1.2 $\mu m^2/s$ and <1 $\mu m^2/s$ suggesting that tumour cellularity is increasing and therefore tumour progression may be evident. This is also true for the GT volume at time point D, as the

percent of restricted tissue is increasing despite the stable visual appearance of T2 hyperintense tissue.

For the case of WWS08, an IDH wild-type, MGMT methylated GBM (Fig. 18), this patient was also diagnosed with PsP at time points C and D. This is supported by the large increase in CE volume with high ADC values (<4 and <1.5 $\mu m^2/s$) and relatively stable volumes of restricted CE tissue (<1.2 and <1 $\mu m^2/s$), suggesting that the CE volume on follow-up MRIs is largely non-restricted tissue. It is also important to note the large increase in GT volume with ADC values <1.2 and <1, which could indicate tumour progression specifically throughout the non-enhancing component of the tumour.

Lastly, Fig.19 depicts the disease timeline of WWS32, an IDH-mutant MGMT methylated GBM diagnosed with tumour recurrence at time point E. This diagnosis is supported both visually and by the increase in CE and GT volumes of tumour tissue with ADC values <1.2 and <1 $\mu m^2/s$. Although progression was diagnosed at time point E, by examining the ADC histograms we can detect increases in restricted CE and GT volumes (ADC <1.2 and <1 $\mu m^2/s$) at time point D compared to time point C. This case highlights a potential role for ADC measures in earlier detection of tumour recurrence.

Statistical comparison of diffusion restricted tissue volumes at various ADC thresholds in patients with PsP versus progression is not possible at this time, due to the limited number of cases with an established clinical diagnosis, as diagnosis of PsP can only be confirmed retrospectively. Further analysis of ADC measures for serial MRIs should be performed with a larger cohort to determine the use of ADC in earlier detection of

tumour recurrence. The benefit of this segmentation protocol is that it is possible to apply the technique to existing clinical datasets of glioma patient MRIs and retrospectively assess ADC in known cases of progression and PsP.

4.3 Correlation with RNA

This study demonstrated significant positive correlations between RNA concentration and diffusion restricted tumour tissue within the CE and GT regions. Specifically, there were significant correlations between the volume of CE tissue with ADC values <1 $\mu m^2/s$, as well as the volume of GT tissue with ADC values <1.2 and <1 $\mu m^2/s$ (Figures 20 and 21). Interestingly there was no significant correlation between RNA concentration and CE or GT tumour volumes, suggesting that RNA concentration is specifically associated with the volume of highly cellular tissue and not the total enhancing or non-enhancing tumour volumes. The strongest correlation with RNA concentration (0.684) was the volume of tissue falling under the 1 $\mu m^2/s$ ADC threshold within the GT ROI. This novel finding highlights that the non-enhancing component of tumour tissue could play a key role in RNA output in GBM.

In the study performed by Osti et al. (2019), it was found that tumour size, as measured on T1w images, did not affect EV output; however, extent of necrosis was negatively correlated with the degree of EV secretion. This finding is consistent with the assumption that viable tumour tissue releases EVs (Osti et al., 2019). Despite this finding, when controlling for level of necrosis by thresholding during the segmentation protocol, it was still found that CE tumour volume does not significantly influence RNA

concentration. By additionally controlling for regions of low cellular density within the CE region and the GT region by applying incremental ADC thresholds, the findings demonstrate that the amount of highly cellular tissue is correlated with RNA output. This captures the idea that two tumours of similar volumes may have different RNA concentrations depending on how cellular each tumour is.

Although these initial findings are promising, it is important to note the small number of patients with available RNA concentrations. Further study using a larger sample size is needed to validate the relationship between tumour cellularity and EV and RNA secretion.

Lastly, RNA concentration could be high when the tumour is extremely cellular or when the BBB is compromised, and it is likely that both factors influence EV output and therefore RNA concentration. If there is a highly cellular tumour with no access to blood vessels, RNA concentration might be low; similarly, if there is a tumour with high perfusion and low cellular density, RNA concentration might also be low.

Differences in perfusion may account for some of the variability in the relationship between ADC and RNA, and controlling for perfusion may lead to a stronger correlation. Therefore, applying this segmentation protocol to perfusion maps of rCBV and rCBF is an important future direction in understanding the relationship between gliomas and EV secretion and subsequently RNA concentration. Similarly, applying this protocol to a larger cohort would allow variables such as MGMT methylation and IDH-mutation status to be controlled for, as these factors may also influence EV secretion.

4.4 EV Analysis

Due to the Covid-19 pandemic, solutions required in the Vn96 capture of EVs were diverted to Covid-19 testing, limiting the capacity to isolate and quantify tumour-derived EVs during this time. A total of 9 patients EV counts for pre-operative MRIs were available; however, quality assurance is still ongoing and the EV data generated to date are not ready for interpretation at this time.

The RNA concentrations were determined to be reliable and therefore were used for further analysis in this thesis. As significant correlations were found between RNA concentration and ADC thresholded volumes, future comparison of EV counts should focus on the following measures: CE volumes with ADC values <1 $\mu m^2/s$ and GT volumes with ADC values <1.2 and <1 $\mu m^2/s$ throughout the disease timeline.

This thesis proposes a reliable method for measuring brain tumour features that is representative of tumour burden. This segmentation protocol could be used to compare patient-derived EV and RNA profiles with changes seen on MRI and to determine if changes in EV and RNA concentrations precede or follow changes on imaging. Therefore, analyzing total RNA content and tumour specific EV concentrations from glioma patient plasma and correlating these longitudinally with the disease course is an important future direction. If these biomarkers correlate with disease state, using EV and RNA profiles could allow regular monitoring of disease progression and treatment effects that is patient specific and minimally invasive. Ultimately, the goal is to develop a

predictive model using both MRI and EV parameters that correlates strongly with tumour behaviour.

4.5 Conclusion

In summary, this study has developed a reliable protocol for quantifying tumour volumes on multiple MRI contrasts using readily available clinical software. This technique can be applied to all serial MRI examinations including post-operative scans with resection cavities in order to assess the volume resected during surgery. Furthermore, this technique overcomes limitations of traditional means for MRI assessment and quantification. My results from applying the segmentation technique to ADC parametric maps demonstrates its potential utility in evaluating diffusion restriction in the longitudinal assessment of tumour behaviour.

For widespread use of this technique in clinical research it will be necessary to evaluate the accuracy of measurements by applying the technique to a realistically generated synthetic dataset of brain tumours with known volumes. Further research with a larger cohort of glioma patients is needed to validate the initial findings of this study and to ensure their generalizability.

APPENDIX A Proof of concept: ROI cloning for Perfusion Imaging Analysis

In order to discern if the same protocol could be applied for perfusion imaging, the GT and CE tumour ROIs were created following the same steps within Brainstat AIF. The ROIs were then cloned to rCBF and rCBV maps (Fig. S1). Thresholding could be completed in a similar fashion as ADC thresholding and can be applied in either direction, depending on what the observer is examining (ie. Volume of tumour tissue that has high perfusion or low perfusion). rCBF and rCBV maps have dimensionless units.

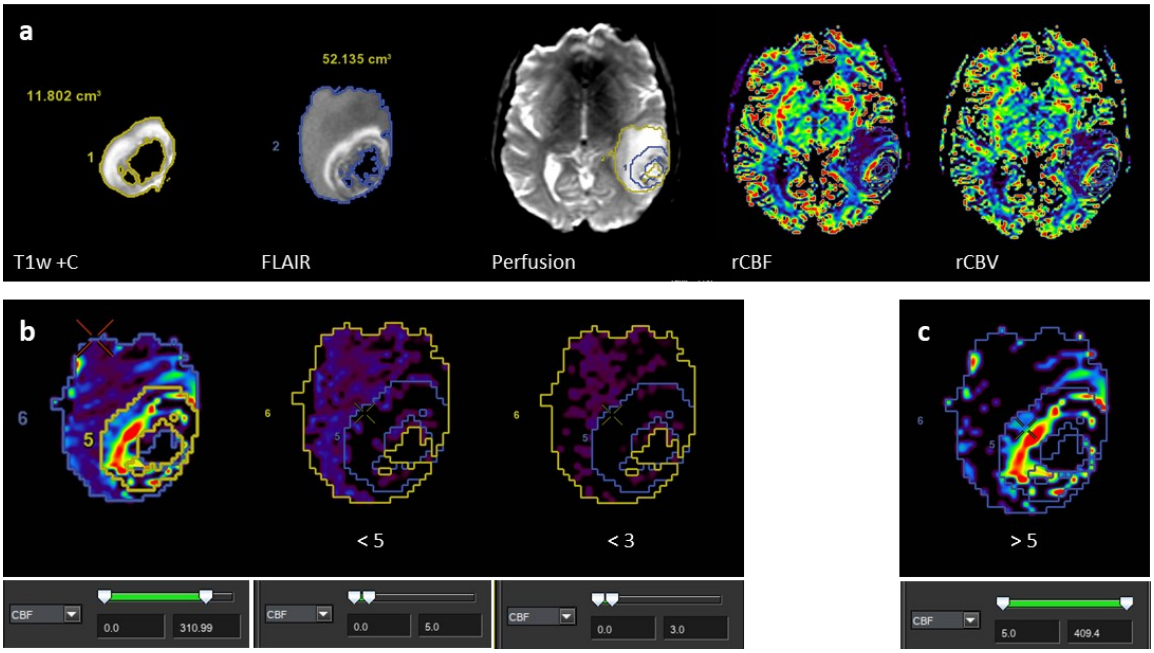

Figure 22. ROI cloning of enhancing and non-enhancing component of a GBM to Perfusion imaging.
a) CE and CT ROI cloned to Perfusion image, rCBF and rCBV parametric maps. b) Example of thresholding using rCBF map, with high cut-offs of <5 and <3 used. c) rCBF map thresholded with a low cut-off of >5.

APPENDIX B Table 5. Patient Demographics and clinical data.

M male, *F* female, *Y* yes, *N* no. Blank cells indicate no available information for the patient in the category.

Patient	Sex	Age	Grade	Pathology	MGMT Methylated (Y/N)	IDH Mutant (Y/N)	ATRX Mutant (Y/N)	1p19q co-deletion (Y/N)	TERT Promoter Mutant	EGFR Amplification
WWS01	F	73	IV	GBM	Y	N				
WWS02	M	63	IV	GBM	N	N				
WWS03	F	71	IV	GBM	Y	N				
WWS04	M	47	III	Oligo	Y	Y	N	Y	Y	N
WWS05	F	67	IV	GBM	N	N				
WWS06	M	56	IV	GBM	N	N	N	N		
WWS07	F	61	IV	GBM	N	N				
WWS08	F	38	IV	GBM	Y	N	N	N	Y	Y
WWS09	M	60	IV	GBM	N	N				
WWS10	F	54	IV	GBM	N	N	N	N	Y	Y
WWS12	F	50	IV	GBM	Y	N				
WWS13	F	36	II	Diffuse Astrocytoma	Y	Y	N	N		
WWS14	M	31	II	Diffuse Astrocytoma	Y	Y	N	N		
WWS15	M	37	II	Diffuse Astrocytoma	N	Y	Y			
WWS16	M	61	IV	GBM	N	N				
WWS18	F	31	II	Diffuse Astrocytoma	Y	Y	Y	N		
WWS20	M	72	IV	GBM	N	N				
WWS21	M	68	IV	GBM	Y	N				
WWS22	M	78	IV	GBM	N	N				
WWS23	F	65	IV	GBM	Y	N				
WWS25	M	78	IV	GBM	Y	N				
WWS26	F	66	IV	GBM	N	N				
WWS27	M	67	IV	GBM	Y	N				
WWS28	M	70	IV	GBM	Y	N				
WWS29	F	60	III	Oligo	Y	Y	N	Y		
WWS30	M	57	IV	GBM	Y	N				
WWS31	M	75	IV	GBM	Y	N				
WWS32	F	38	IV	GBM	Y	Y	Y	N		
WWS33	M	64	IV	GBM	Y	N				
WWS36	F	66	III	NOS	Y	N	N	N	N	N
WWS37	M	38	II	Diffuse Astrocytoma	Y	Y	Y	N		
WWS38	M	60	IV	GBM	N	N				
WWS39	M	37	IV	GBM	N	Y				
WWS40	M	56	IV	GBM	Y	N	N	N	Y	Y

BIBLIOGRAPHY

Abler, D., Sahoo, P., Kingsmore, K., Munson, J., Büchler, P., Rockne, R., Stine, C., Chase Cornelison, R., Macapagal, J., Park, T., Joret, M., Rustenhoven, J., Dieriks, B., Faull, R., Schweder, P., & Dragunow, M. (2018). Tmic-19. Using Quantitative Mr Imaging to Relate GBM Mass Effect to Perfusion and Diffusion Characteristics of the Tumor Micro-Environment. *Neuro-Oncology*, *20*(6), vi260–vi260.

Ahir, B. K., Engelhard, H. H., & Lakka, S. S. (2020). Tumor Development and Angiogenesis in Adult Brain Tumor: Glioblastoma. *Molecular Neurobiology 2020 57:5*, *57*(5), 2461–2478.

Ameratunga, M., Pavlakis, N., Wheeler, H., Grant, R., Simes, J., & Khasraw, M. (2018). Anti-angiogenic therapy for high-grade glioma. In *Cochrane Database of Systematic Reviews, 18*(11).

Argentieri, C., Zochowski, C., Braun, W., Burge, J., & Potter, G. (2020). Evidence-Based Management of Complex Knee Injuries E-Book: Restoring the Anatomy to Achieve Best Outcomes, *MRI Basics 29*.

Balakrishnan, A., Schuurmans, C., Roy, S., Fleming, T., & Leong, H. S. (2020). The emerging role of extracellular vesicles in the glioma microenvironment: Biogenesis and clinical relevance. In *Cancers, 12*(7).

Bitar, R., Leung, G., Perng, R., Tadros, S., Moody, A. R., Sarrazin, J., McGregor, C., Christakis, M., Symons, S., Nelson, A., & Roberts, T. P. (2006). MR pulse sequences: What every radiologist wants to know but is afraid to ask. In *Radiographics, 26*(2).

Brandes, A. A., Franceschi, E., Tosoni, A., Blatt, V., Pession, A., Tallini, G., Bertorelle, R., Bartolini, S., Calbucci, F., Andreoli, A., Frezza, G., Leonardi, M., Spagnolli, F., & Ermani, M. (2008). MGMT promoter methylation status can predict the incidence and outcome of pseudoprogression after concomitant radiochemotherapy in newly diagnosed glioblastoma patients. *Journal of Clinical Oncology*, *26*(13).

Central Nervous System: Progress of Today and a Preview of Tomorrow: The Cancer Genome Atlas Research Network. Comprehensive, integrative genomic analysis of diffuse lower-grade gliomas. New Engl J Med 2015. (5). (2016). In *International Journal of Radiation Oncology Biology Physics, 94*(3).

Chai, R., Li, G., Liu, Y., Zhang, K., Zhao, Z., Wu, F., Chang, Y., Pang, B., Li, J., Li, Y., Jiang, T., & Wang, Y. (2021). Predictive value of MGMT promoter methylation on the survival of TMZ treated IDH-mutant glioblastoma. *Cancer Biology and Medicine*, *18*(1).

Chamberlain, M. C., Glantz, M. J., Chalmers, L., van Horn, A., & Sloan, A. E. (2007). Early necrosis following concurrent Temodar and radiotherapy in patients with glioblastoma. *Journal of Neuro-Oncology*, *82*(1).

Chukwueke, U. N., & Wen, P. Y. (2019). Use of the Response Assessment in Neuro-Oncology (RANO) criteria in clinical trials and clinical practice. *CNS Oncology*, *8*(1).

Curran, W. J., Scott, C. B., Horton, J., Nelson, J. S., Weinstein, A. S., Fischbach, A. J., Chang, C. H., Rotman, M., Asbell, S. O., Krisch, R. E., & Nelson, D. F. (1993). Recursive partitioning analysis of prognostic factors in three radiation therapy oncology group malignant glioma trials. *Journal of the National Cancer Institute*, *85*(9).

Czernek, L., & Düchler, M. (2017). Functions of Cancer-Derived Extracellular Vesicles in Immunosuppression. In *Archivum Immunologiae et Therapiae Experimentalis, 65*(4).

Dalesandro, M. F., & Andre, J. B. (2016). Posttreatment Evaluation of Brain Gliomas. In *Neuroimaging Clinics of North America, 26*(4).

Dallabona, M., Sarubbo, S., Merler, S., Corsini, F., Pulcrano, G., Rozzanigo, U., Barbareschi, M., & Chioffi, F. (2017). Impact of mass effect, tumor location, age, and surgery on the cognitive outcome of patients with high-grade gliomas: A longitudinal study. *Neuro-Oncology Practice*, *4*(4).

Darbar, A., Waqas, M., Enam, S. F., & Mahmood, S. D. (2018). Use of Preoperative Apparent Diffusion Coefficients to Predict Brain Tumor Grade. *Cureus*.

Doyle, L., & Wang, M. (2019). Overview of Extracellular Vesicles, Their Origin, Composition, Purpose, and Methods for Exosome Isolation and Analysis. *Cells*, *8*(7).

El-Hateer, H., Souhami, L., Roberge, D. D., del Maestro, R., Leblanc, R., Eldebawy, E., Muanza, T., Melançon, D., Kavan, P., & Guiot, M. C. (2009). Low-grade oligodendroglioma: An indolent but incurable disease? - Clinical article. *Journal of Neurosurgery*, *111*(2).

Essig, M., Shiroishi, M. S., Nguyen, T. B., Saake, M., Provenzale, J. M., Enterline, D., Anzalone, N., Doŕfler, A., Rovira, À., Wintermark, M., & Law, M. (2013). Perfusion MRI: The five most frequently asked technical questions. In *American Journal of Roentgenology, 200*(1).

Gering, D., Kotrotsou, A., Young-Moxon, B., Miller, N., Avery, A., Kohli, L., Knapp, H., Hoffman, J., Chylla, R., Peitzman, L., & Mackie, T. R. (2020). Measuring Efficiency of Semi-automated Brain Tumor Segmentation by Simulating User Interaction. *Frontiers in Computational Neuroscience*, *14*.

Good, D. J., Polverini, P. J., Rastinejad, F., le Beau, M. M., Lemons, R. S., Frazier, W. A., & Bouck, N. P. (1990). A tumor suppressor-dependent inhibitor of angiogenesis is immunologically and functionally indistinguishable from a fragment of thrombospondin. *Proceedings of the National Academy of Sciences of the United States of America*, *87*(17).

Goodenberger, M. L., & Jenkins, R. B. (2012). Genetics of adult glioma. In *Cancer Genetics, 205*(12).

Hallal, S., Ebrahimkhani, S., Shivalingam, B., Graeber, M. B., Kaufman, K. L., & Buckland, M. E. (2019). The emerging clinical potential of circulating extracellular vesicles for non-invasive glioma diagnosis and disease monitoring. In *Brain Tumor Pathology, 36*(2).

Hamamci, A., Kucuk, N., Karaman, K., Engin, K., & Unal, G. (2012). Tumor-cut: Segmentation of brain tumors on contrast enhanced mr images for radiosurgery applications. *IEEE Transactions on Medical Imaging*, *31*(3).

Hasselblatt, M., Jaber, M., Reuss, D., Grauer, O., Bibo, A., Terwey, S., Schick, U., Ebel, H., Niederstadt, T., Stummer, W., von Deimling, A., & Paulus, W. (2018). Diffuse astrocytoma, IDH-wildtype: A dissolving diagnosis. *Journal of Neuropathology and Experimental Neurology*, *77*(6).

Hilario, A., Ramos, A., Perez-Nuñez, A., Salvador, E., Millan, J. M., Lagares, A., Sepulveda, J. M., Gonzalez-Leon, P., Hernandez-Lain, A., & Ricoy, J. R. (2012). The added value of apparent diffusion coefficient to cerebral blood volume in the preoperative grading of diffuse gliomas. *American Journal of Neuroradiology*, *33*(4). https://doi.org/10.3174/ajnr.A2846

Hygino Da Cruz, L. C., Rodriguez, I., Domingues, R. C., Gasparetto, E. L., & Sorensen, A. G. (2011). Pseudoprogression and pseudoresponse: Imaging challenges in the assessment of posttreatment glioma. In *American Journal of Neuroradiology, 32*(11).

Ibrahim, M. A., Emerson, J. F., & Cotman, C. W. (1998). Magnetic resonance imaging relaxation times and gadolinium-DPTA relaxivity values in human cerebrospinal fluid. *Investigative Radiology*, *33*(3).

Jenkinson, M. D., du Plessis, D. G., Smith, T. S., Joyce, K. A., Warnke, P. C., & Walker, C. (2006). Histological growth patterns and genotype in oligodendroglial tumours: Correlation with MRI features. *Brain*, *129*(7).

Juratli, T. A., Tummala, S. S., Riedl, A., Daubner, D., Hennig, S., Penson, T., Zolal, A., Thiede, C., Schackert, G., Krex, D., Miller, J. J., & Cahill, D. P. (2019). Radiographic assessment of contrast enhancement and T2/FLAIR mismatch sign in lower grade gliomas: correlation with molecular groups. *Journal of Neuro-Oncology*, *141*(2).

Kim, W. Y., & Lee, H. Y. (2009). Brain angiogenesis in developmental and pathological processes: Mechanism and therapeutic intervention in brain tumors. In *FEBS Journal, 276*(17).

Klein, M. (2012). Neurocognitive functioning in adult WHO grade II gliomas: Impact of old and new treatment modalities. *Neuro-Oncology*, *14*(4).

Komori, T. (2017). The 2016 WHO classification of tumours of the central nervous system: The major points of revision. In *Neurologia Medico-Chirurgica, 57*(7).

Kono, K., Inoue, Y., Nakayama, K., Shakudo, M., Morino, M., Ohata, K., Wakasa, K., & Yamada, R. (2001). The role of diffusion-weighted imaging in patients with brain tumors. *American Journal of Neuroradiology*, *22*(6).

Krex, D., Klink, B., Hartmann, C., von Deimling, A., Pietsch, T., Simon, M., Sabel, M., Steinbach, J. P., Heese, O., Reifenberger, G., Weller, M., & Schackert, G. (2007). Long-term survival with glioblastoma multiforme. *Brain*, *130*(10).

Kwee, T. C., Galbán, C. J., Tsien, C., Junck, L., Sundgren, P. C., Ivancevic, M. K., Johnson, T. D., Meyer, C. R., Rehemtulla, A., Ross, B. D., & Chenevert, T. L. (2010). Comparison of apparent diffusion coefficients and distributed diffusion coefficients in high-grade gliomas. *Journal of Magnetic Resonance Imaging*, *31*(3).

Lacroix, M., Abi-Said, D., Fourney, D. R., Gokaslan, Z. L., Shi, W., DeMonte, F., Lang, F. F., McCutcheon, I. E., Hassenbusch, S. J., Holland, E., Hess, K., Michael, C., Miller, D., & Sawaya, R. (2001). A multivariate analysis of 416 patients with glioblastoma multiforme: Prognosis, extent of resection, and survival. *Journal of Neurosurgery*, *95*(2).

Leao, D. J., Craig, P. G., Godoy, L. F., Leite, C. C., & Policeni, B. (2020). Response assessment in neuro-oncology criteria for gliomas: Practical approach using conventional and advanced techniques. In *American Journal of Neuroradiology, 41*(1).

Lee, W. J., Choi, S. H., Park, C. K., Yi, K. S., Kim, T. M., Lee, S. H., Kim, J. H., Sohn, C. H., Park, S. H., & Kim, I. H. (2012). Diffusion-weighted MR Imaging for the Differentiation of True Progression from Pseudoprogression Following Concomitant Radiotherapy with Temozolomide in Patients with Newly Diagnosed High-grade Gliomas. *Academic Radiology*, *19*(11).

Louis, D. N., Ohgaki, H., Wiestler, O. D., Cavenee, W. K., Burger, P. C., Jouvet, A., Scheithauer, B. W., & Kleihues, P. (2007). The 2007 WHO classification of tumours of the central nervous system. *Acta Neuropathologica, 114*(2).

Louis, D. N., Perry, A., Reifenberger, G., von Deimling, A., Figarella-Branger, D., Cavenee, W. K., Ohgaki, H., Wiestler, O. D., Kleihues, P., & Ellison, D. W. (2016). The 2016 World Health Organization Classification of Tumors of the Central Nervous System: a summary. *Acta Neuropathologica, 131*(6).

Louis, D. N., Perry, A., Wesseling, P., Brat, D. J., Cree, I. A., Figarella-Branger, D., Hawkins, C., Ng, H. K., Pfister, S. M., Reifenberger, G., Soffietti, R., von Deimling, A., & Ellison, D. W. (2021). The 2021 WHO classification of tumors of the central nervous system: A summary. *Neuro-Oncology*, *23*(8).

Mastrogiacomo, S., Dou, W., Jansen, J. A., & Walboomers, X. F. (2019). Magnetic Resonance Imaging of Hard Tissues and Hard Tissue Engineered Bio-substitutes. *Molecular Imaging and Biology, 21*(6).

McKinnon, C., Nandhabalan, M., Murray, S. A., & Plaha, P. (2021). Glioblastoma: Clinical presentation, diagnosis, and management. *The BMJ, 374*.

Menze, B. H., Jakab, A., Bauer, S., Kalpathy-Cramer, J., Farahani, K., Kirby, J., Burren, Y., Porz, N., Slotboom, J., Wiest, R., Lanczi, L., Gerstner, E., Weber, M. A., Arbel, T., Avants, B. B., Ayache, N., Buendia, P., Collins, D. L., Cordier, N., van Leemput, K. (2015). The Multimodal Brain Tumor Image Segmentation Benchmark (BRATS). *IEEE Transactions on Medical Imaging*, *34*(10).

Mitra, J., Nayate, A., Madabhushi, A., & Tiwari, P. (2016). Nimg-51. Impact on Remote Functional Areas due to Tumor Mass Effect is Prognostic of Overall Survival in Glioblastoma Multiforme. *Neuro-Oncology*, *18*(6).

Onizuka, H., Masui, K., & Komori, T. (2020). Diffuse gliomas to date and beyond 2016 WHO Classification of Tumours of the Central Nervous System. *International Journal of Clinical Oncology, 25*(6).

Orlandi, M., Botti, A., Sghedoni, R., Cagni, E., Ciammella, P., Iotti, C., & Iori, M. (2016). Feasibility of voxel-based Dose Painting for recurrent Glioblastoma guided by ADC values of Diffusion-Weighted MR imaging. *Physica Medica*, *32*(12).

Osti, D., Bene, M. del, Rappa, G., Santos, M., Matafora, V., Richichi, C., Faletti, S., Beznoussenko, G. v., Mironov, A., Bachi, A., Fornasari, L., Bongetta, D., Gaetani, P., DiMeco, F., Lorico, A., & Pelicci, G. (2019). Clinical significance of extracellular vesicles in plasma from glioblastoma patients. *Clinical Cancer Research*, *25*(1).

Ostrom, Q. T., Gittleman, H., Farah, P., Ondracek, A., Chen, Y., Wolinsky, Y., Stroup, N. E., Kruchko, C., & Barnholtz-Sloan, J. S. (2013). CBTRUS statistical report: Primary brain and central nervous system tumors diagnosed in the United States in 2006-2010. *Neuro-Oncology*, *15*(2).

Ostrom, Q. T., Gittleman, H., Truitt, G., Boscia, A., Kruchko, C., & Barnholtz-Sloan, J. S. (2018). CBTRUS statistical report: Primary brain and other central nervous system tumors diagnosed in the United States in 2011-2015. In *Neuro-Oncology, 20*.

Ostrom, Q. T., Patil, N., Cioffi, G., Waite, K., Kruchko, C., & Barnholtz-Sloan, J. S. (2020). CBTRUS statistical report: Primary brain and other central nervous system tumors diagnosed in the United States in 2013-2017. *Neuro-Oncology*, *22*(1).

Palombi, L., Marchetti, P., Salvati, M., Osti, M. F., Frati, L., & Frati, A. (2018). Interventions to reduce neurological symptoms in patients with GBM receiving radiotherapy: From theory to clinical practice. *Anticancer Research*, *38*(4).

Pooja, V., Kumar, M. K., & Kamalesh, K. (2021). Comparative analysis of segmentation techniques on MRI brain tumor images. *Materials Today: Proceedings*, *47*.

Pope, W. B., Sayre, J., Perlina, A., Villablanca, J. P., Mischel, P. S., & Cloughesy, T. F. (2005). MR imaging correlates of survival in patients with high-grade gliomas. *American Journal of Neuroradiology*, *26*(10).

Porz, N., Bauer, S., Pica, A., Schucht, P., Beck, J., Verma, R. K., Slotboom, J., Reyes, M., & Wiest, R. (2014). Multi-modal glioblastoma segmentation: Man versus machine. *PLoS ONE*, *9*(5).

Rabinov, J. D., Lee, P. L., Barker, F. G., Louis, D. N., Harsh IV, G. R., Cosgrove, G. R., Chiocca, E. A., Thornton, A. F., Loeffler, J. S., Henson, J. W., & Gonzalez, R. G. (2002). In vivo 3-T MR spectroscopy in the distinction of recurrent glioma versus radiation effects: Initial experience. *Radiology*, *225*(3).

Rank, A., Nieuwland, R., Crispin, A., Grützner, S., Iberer, M., Toth, B., & Pihusch, R. (2011). Clearance of platelet microparticles in vivo. *Platelets*, *22*(2).

Reifenberger, G., Wirsching, H. G., Knobbe-Thomsen, C. B., & Weller, M. (2017). Advances in the molecular genetics of gliomas-implications for classification and therapy. In *Nature Reviews Clinical Oncology, 14*(7).

Reimer, C., Deike, K., Graf, M., Reimer, P., Wiestler, B., Omar Floca, R., Kickingereder, P., Schlemmer, H. P., Wick, W., Bendszus, M., & Radbruch, A. (2017). Differentiation of pseudoprogression and real progression in glioblastoma using ADC parametric response maps. *PLoS ONE*, *12*(4).

Rooj, A. K., Mineo, M., & Godlewski, J. (2016). MicroRNA and extracellular vesicles in glioblastoma: small but powerful. *Brain Tumor Pathology*, *33*(2).

Saenz-Antoñanzas, A., Auzmendi-Iriarte, J., Carrasco-Garcia, E., Moreno-Cugnon, L., Ruiz, I., Villanua, J., Egaña, L., Otaegui, D., Samprón, N., & Matheu, A. (2019). Liquid biopsy in glioblastoma: Opportunities, applications and challenges. *Cancers, 11*(7).

Santangelo, A., Imbrucè, P., Gardenghi, B., Belli, L., Agushi, R., Tamanini, A., Munari, S., Bossi, A. M., Scambi, I., Benati, D., Mariotti, R., di Gennaro, G., Sbarbati, A., Eccher, A., Ricciardi, G. K., Ciceri, E. M., Sala, F., Pinna, G., Lippi, G., Dechecchi, M. C. (2018). A microRNA signature from serum exosomes of patients with glioma as complementary diagnostic biomarker. *Journal of Neuro-Oncology*, *136*(1).

Schapira, A. H. V. (2007). Neurology and clinical neuroscience. In *Neurology and Clinical Neuroscience*.

Schoenegger, K., Oberndorfer, S., Wuschitz, B., Struhal, W., Hainfellner, J., Prayer, D., Heinzl, H., Lahrmann, H., Marosi, C., & Grisold, W. (2009). Peritumoral edema on MRI at initial diagnosis: An independent prognostic factor for glioblastoma? *European Journal of Neurology*, *16*(7).

Seeger, A., Braun, C., Skardelly, M., Paulsen, F., Schittenhelm, J., Ernemann, U., & Bisdas, S. (2013). Comparison of Three Different MR Perfusion Techniques and MR Spectroscopy for Multiparametric Assessment in Distinguishing Recurrent High-Grade Gliomas from Stable Disease. *Academic Radiology*, *20*(12).

Sharma, H. A. (2009). MRI physics-basic principles. *Acta Neuropsychiatrica, 21*(4).

Shields, L. B. E., Shelton, B. J., Shearer, A. J., Chen, L., Sun, D. A., Parsons, S., Bourne, T. D., LaRocca, R., & Spalding, A. C. (2015). Dexamethasone administration during definitive radiation and temozolomide renders a poor prognosis in a retrospective analysis of newly diagnosed glioblastoma patients. *Radiation Oncology*, *10*(1).

Simon, T., Jackson, E., & Giamas, G. (2020). Breaking through the glioblastoma micro-environment via extracellular vesicles. *Oncogene, 39*(23).

Siravegna, G., Mussolin, B., Venesio, T., Marsoni, S., Seoane, J., Dive, C., Papadopoulos, N., Kopetz, S., Corcoran, R. B., Siu, L. L., & Bardelli, A. (2019). How liquid biopsies can change clinical practice in oncology. *Annals of Oncology, 30*(10).

Skog, J., Würdinger, T., van Rijn, S., Meijer, D. H., Gainche, L., Curry, W. T., Carter, B. S., Krichevsky, A. M., & Breakefield, X. O. (2008). Glioblastoma microvesicles transport RNA and proteins that promote tumour growth and provide diagnostic biomarkers. *Nature Cell Biology*, *10*(12).

Smith, T., Yuan, Y., Emily, W., & Davis, F. (2019). Brain Tumour Registry of Canada (BTRC): Incidence Report 2010-2015. In *Brain Tumour Registry of Canada (BTRC) A Surveillance Research Collaborative*.

Stupp, R., Hegi, M. E., Mason, W. P., van den Bent, M. J., Taphoorn, M. J., Janzer, R. C., Ludwin, S. K., Allgeier, A., Fisher, B., Belanger, K., Hau, P., Brandes, A. A., Gijtenbeek, J., Marosi, C., Vecht, C. J., Mokhtari, K., Wesseling, P., Villa, S., Eisenhauer, E., Mirimanoff, R. O. (2009). Effects of radiotherapy with concomitant and adjuvant temozolomide versus radiotherapy alone on survival in glioblastoma in a randomised phase III study: 5-year analysis of the EORTC-NCIC trial. *The Lancet Oncology*, *10*(5).

Stupp, R., Mason, W. P., van den Bent, M. J., Weller, M., Fisher, B., Taphoorn, M. J. B., Belanger, K., Brandes, A. A., Marosi, C., Bogdahn, U., Curschmann, J., Janzer, R. C., Ludwin, S. K., Gorlia, T., Allgeier, A., Lacombe, D., Cairncross, J. G., Eisenhauer, E., & Mirimanoff, R. O. (2005). Radiotherapy plus Concomitant and Adjuvant Temozolomide for Glioblastoma. *New England Journal of Medicine*, *352*(10).

Suh, C. H., Kim, H. S., Jung, S. C., Choi, C. G., & Kim, S. J. (2018). Clinically relevant imaging features for MGMT promoter methylation in multiple glioblastoma studies: A systematic review and meta-analysis. *American Journal of Neuroradiology*, *39*(8).

Tankov, S., & Walker, P. R. (2021). Glioma-Derived Extracellular Vesicles – Far More Than Local Mediators. In *Frontiers in Immunology, 12*.

Tervonen, O., Forbes, G., Scheithauer, B. W., & Dietz, M. J. (1992). Diffuse “fibrillary” astrocytomas: correlation of MRI features with histopathologic parameters and tumor grade. *Neuroradiology*, *34*(3).

Tolia, M., Verganelakis, D., Tsoukalas, N., Kyrgias, G., Papathanasiou, M., Mosa, E., Kokakis, I., Kouvaris, J. R., Pissakas, G., Pistevou-Gombaki, K., Kelekis, N., & Kouloulias, V. (2015). Prognostic value of MRS metabolites in postoperative irradiated high-grade gliomas. *BioMed Research International*, *2015*.

Tozer, D. J., Jäger, H. R., Danchaivijitr, N., Benton, C. E., Tofts, P. S., Rees, J. H., & Waldman, A. D. (2007). Apparent diffusion coefficient histograms may predict low-grade glioma subtype. *NMR in Biomedicine*, *20*(1).

Urbanska, K., Sokolowska, J., Szmidt, M., & Sysa, P. (2014). Glioblastoma multiforme - An overview. In *Wspolczesna Onkologia, 18*(5).

van den Bent, M. J., Reni, M., Gatta, G., & Vecht, C. (2008). Oligodendroglioma. *Critical Reviews in Oncology/Hematology*, *66*(3), 262–272.

van Dijken, B. R. J., van Laar, P. J., Holtman, G. A., & van der Hoorn, A. (2017). Diagnostic accuracy of magnetic resonance imaging techniques for treatment response evaluation in patients with high-grade glioma, a systematic review and meta-analysis. *European Radiology*, *27*(10).

van Kempen, E. J., Post, M., Mannil, M., Witkam, R. L., ter Laan, M., Patel, A., Meijer, F. J. A., & Henssen, D. (2021). Performance of machine learning algorithms for glioma segmentation of brain MRI: a systematic literature review and meta-analysis. In *European Radiology, 31*(12).

van Linde, M. E., Brahm, C. G., de Witt Hamer, P. C., Reijneveld, J. C., Bruynzeel, A. M. E., Vandertop, W. P., van de Ven, P. M., Wagemakers, M., van der Weide, H. L., Enting, R. H., Walenkamp, A. M. E., & Verheul, H. M. W. (2017). Treatment outcome of patients with recurrent glioblastoma multiforme: a retrospective multicenter analysis. *Journal of Neuro-Oncology*, *135*(1).

Wadhwa, A., Bhardwaj, A., & Singh Verma, V. (2019). A review on brain tumor segmentation of MRI images. In *Magnetic Resonance Imaging, 61*.

Wang, T. J. C., & Mehta, M. P. (2019). Low-Grade Glioma Radiotherapy Treatment and Trials. In *Neurosurgery Clinics of North America, 30*(1).

Watanabe, M., Tanaka, R., & Takeda, N. (1992). Magnetic resonance imaging and histopathology of cerebral gliomas. *Neuroradiology*, *34*(6).

Weller, M., Stupp, R., Reifenberger, G., Brandes, A. A., van den Bent, M. J., Wick, W., & Hegi, M. E. (2010). MGMT promoter methylation in malignant gliomas: Ready for personalized medicine? In *Nature Reviews Neurology, 6*(1).

Weller, M., Tabatabai, G., Kästner, B., Felsberg, J., Steinbach, J. P., Wick, A., Schnell, O., Hau, P., Herrlinger, U., Sabel, M. C., Wirsching, H. G., Ketter, R., Bähr, O., Platten, M., Tonn, J. C., Schlegel, U., Marosi, C., Goldbrunner, R., Stupp, R., Reifenberger, G. (2015). MGMT promoter methylation is a strong prognostic biomarker for benefit from dose-intensified temozolomide rechallenge in progressive Glioblastoma: The DIRECTOR Trial. *Clinical Cancer Research*, *21*(9).

Weller, M., van den Bent, M., Preusser, M., le Rhun, E., Tonn, J. C., Minniti, G., Bendszus, M., Balana, C., Chinot, O., Dirven, L., French, P., Hegi, M. E., Jakola, A. S., Platten, M., Roth, P., Rudà, R., Short, S., Smits, M., Taphoorn, M. J. B., Wick, W. (2021). EANO guidelines on the diagnosis and treatment of diffuse gliomas of adulthood. *Nature Reviews Clinical Oncology*, *18*(3).

Werner, J. M., Stoffels, G., Lichtenstein, T., Borggrefe, J., Lohmann, P., Ceccon, G., Shah, N. J., Fink, G. R., Langen, K. J., Kabbasch, C., & Galldiks, N. (2019). Differentiation of treatment-related changes from tumour progression: a direct comparison between dynamic FET PET and ADC values obtained from DWI MRI. *European Journal of Nuclear Medicine and Molecular Imaging*, *46*(9).

Westbrook, C., & Talbot, J. (2019). MRI in Practice 5th. In *John Wiley & Sons Ltd*.

Wick, W., Meisner, C., Hentschel, B., Platten, M., Schilling, A., Wiestler, B., Sabel, M. C., Koeppen, S., Ketter, R., Weiler, M., Tabatabai, G., von Deimling, A., Gramatzki, D., Westphal, M., Schackert, G., Loeffler, M., Simon, M., Reifenberger, G., & Weller, M. (2013). Prognostic or predictive value of MGMT promoter methylation in gliomas depends on IDH1 mutation. *Neurology*, *81*(17).

Wick, W., Weller, M., van den Bent, M., Sanson, M., Weiler, M., von Deimling, A., Plass, C., Hegi, M., Platten, M., & Reifenberger, G. (2014). MGMT testing - The challenges for biomarker-based glioma treatment. In *Nature Reviews Neurology, 10*(7).

Xavier, C. P. R., Caires, H. R., Barbosa, M. A. G., Bergantim, R., Guimarães, J. E., & Vasconcelos, M. H. (2020). The Role of Extracellular Vesicles in the Hallmarks of Cancer and Drug Resistance. In *Cells, 9*(5).

Yang, D. (2014). Standardized MRI assessment of high-grade glioma response: A review of the essential elements and pitfalls of the RANO criteria. *Neuro-Oncology Practice*, *3*(1).

Yekula, A., Yekula, A., Muralidharan, K., Kang, K., Carter, B. S., & Balaj, L. (2019). Extracellular Vesicles in Glioblastoma Tumor Microenvironment. In *Frontiers in Immunology, 10.*

Yip, S., Butterfield, Y. S., Morozova, O., Chittaranjan, S., Blough, M. D., An, J., Birol, I., Chesnelong, C., Chiu, R., Chuah, E., Corbett, R., Docking, R., Firme, M., Hirst, M., Jackman, S., Karsan, A., Li, H., Louis, D. N., Maslova, A., Marra, M. A. (2012). Concurrent CIC mutations, IDH mutations, and 1p/19q loss distinguish oligodendrogliomas from other cancers. *Journal of Pathology*, *226*(1).

Young, G. S. (2007). Advanced MRI of Adult Brain Tumors. *Neurologic Clinics, 25*(4).